Exploring microstructure refinement and deformation mechanisms in severely deformed LPBF AlSi10Mg alloy

Przemyslaw Snopiński

Exploring microstructure refinement and deformation mechanisms in severely deformed LPBF AlSi10Mg alloy

P. Snopiński[1,*]

[1] *Department of Engineering Materials and Biomaterials, Silesian University of Technology, 18A Konarskiego Street, 44-100 Gliwice, Poland;*
**corresponding author e-mail: przemyslaw.snopinski@polsl.pl*

Abstract

An additively produced AlSi10Mg aluminium alloy was post-processed by Equal Channel Angular pressing at 150 ºC. This resulted in a fabrication of the novel submicrometer-grained (SMG) microstructure, which was subsequently characterised by optical microscopy, scanning electron microscopy, and transmission electron microscopy. In addition, the deformation mechanisms were also studied in detail at different scales. The post-deformation studies show that the predominant deformation mechanism of the alloy matrix was dislocation slip. However, the heterogeneous microstructure also activated another important mesoscale deformation mechanism - the plastic deformation gradient (incompatible deformation) that existed between the boundaries of the melt pools and their interiors and the Al/Si interfaces. More importantly, the TEM analysis provided evidence for the deformation twinning of the hard Si phase as well as for the deformation-induced amorphisation of the Si phase. The revealed synergy of different deformation modes sheds light on the good balance between strength and ductility and opens a new horizon for the development of the next generation of structural materials.

Keywords: Aluminium alloy, Additive manufacturing, Laser powder bed fusion (LPBF), Equal Channel Angular Pressing, Grain refinement, Deformation mechanisms, Dislocation slip, Twinning, Solid-State amorphisation, Incompatible deformation.

1. Introduction

In recent decades, the accelerated development of the aerospace and transportation sectors has led to significant changes in the global climate due to ever-increasing CO2 emissions [1] [2]. Although growing political awareness and economic necessity have driven research and development in these sectors, current technologies are not yet able to fully address this challenge. One way to significantly improve energy savings and thus reduce harmful greenhouse gas emissions is to significantly optimize vehicle design, which is strongly related to the materials used. Reducing weight by using low-density materials, such as magnesium or aluminuim alloys, instead of high-density steel is a proven approach to reducing greenhouse gas emissions. Vehicle weight reduction leads linearly to a corresponding reduction in fuel consumption, with a general value of 0.5 liters less fuel per 100 kg weight reduction [3]. Unfortunately, numerous operational requirements and technical criteria, particularly those promoting strength and ductility, limit the benefits of weight reduction due to the limited property portfolio of commercially available aluminium alloys and require the unfavourable use of a multi-material mix, limiting recyclability at the end of the product life. Therefore, the trade-off between strength and ductility becomes a fundamental challenge in the fabrication of high performance lightweight structural materials [4].

When it comes to metals, the strength is increased mainly by refining the microstructure down to the nanometer scale, solid solution, dislocation (cold work) and precipitation (second-phase particle)

hardening [5] [6]. However, these strategies are often accompanied by a reduction in ductility [7] due to the lack of strain hardening capacity, which is primarily due to inefficient storage of dislocations. According to Considère's criterion for tensile testing, to obtain a large uniform elongation (retarding localized deformation or necking phenomenon), a high strain hardening rate and a material with high dislocation storage are required [8]. Therefore, microstructures that exhibit a high strain hardening capacity are of particular interest.

As mentioned above, the key principle for achieving synergistic effects between strength and ductility is that the microstructure should be designed to sufficiently promote the uniformity of plastic flow by delocalizing "localized" strains [4]. For metallic materials with homogeneous microstructure, the current strategy is to maximize dislocation motion (suppress localized dislocation pile-up) through high entropy effect [9] or alloying [10]. Another approach is to develop a heterogeneous (gradient) structure originating from biological material [11], for example, a bimodal/gradient/laminated structure [12] [13]. The strain hardening enhancement due to heterogeneous microstructure design results from the long-range inter-granular back stress strengthening as observed in many heterogeneous materials [14] [15].

In numerous references [16] [17] [18] [19] [20], it has been shown that laser powder bed-formed alloys (LPBF) represent a novel group of metallic materials with unique heterogeneous microstructures and deformation mechanisms that differ significantly from their cast counterparts. Considering lightweight SLM materials, most recent research has focused on titanium alloys [21], steel and iron alloys [22], nickel alloys [23], high entropy [24], and aluminium alloys [25]. Among the aluminium alloys used in additive manufacturing, hypoeutectic Al-SI alloys have been studied quite intensively due to their high specific strength, good electrical and thermal conductivity, good weldability, and corrosion resistance [26] [27] [28]. This group of alloys has been primarily represented by the AlSi10Mg alloy, which has been the most frequently investigated DMLS alloy in recent years, probably due to its ease of processing. Obviously, the microstructure of the DLMS alloy AlSi10Mg is "plastically inhomogeneous", that is, it consists of interfaces with stronger and weaker plastic deformation capability ("harder" and "softer" regions/phases) [29]. The first one is the Si phase with cellular morphology and the second one is the melt pool boundary (heat affected zone) [30] [31]. Moreover, the presence of a strain gradient, the "hard" Si and "soft" Al phases, leads to strain partitioning between them during straining, activating additional deformation modes, for example, deformation twins in a harder phase [32], which increase dislocation storage capacity and can be used to improve ductility. Therefore, LPBF AlSi10Mg alloy has a work-hardening exponent of ~0.252, which is almost twice that of PM alloy (~0.127) and more than twice that of the gravity-cast alloy (~0.1) [33], making it an ideal material to overcome the "holy grail" of materials science, the trade-off between strength and ductility.

Recently, a novel concept of heterogeneous nanostructured materials (characterised by an unusually small length scale of the plastic deformation gradient) has been proposed to achieve unprecedented mechanical properties [34]. This is because deformation mechanisms that work at the micrometre scale are not applicable at nanometer length scales. For example, recent studies have shown that deformation twinning is very sensitive to the size effect [35] [36]. In many cases, DT is more pronounced in nanocrystalline materials than in their coarse-grained counterparts [37].

In view of the above considerations, the author believes that one of the most studied methods of severe plastic deformation (SPD)-equal channel angular pressing (ECAP)-deserves greater attention from the additive manufacturing industry. This technique has been used for several decades to refine the microstructure of metallic materials [38], and as recently reported [32] [39], the combination of

both methods can lead to exceptional mutually exclusive properties of AM parts, namely high strength with reasonable ductility.

Although several studies and publications have been carried out on the deformation mechanisms of Al-Si alloys produced by AM [40] [41], no attempt has been made to investigate the deformation micromechanisms in SPD-processed samples. Therefore, the main objective of this work is to further investigate the underlying plastic deformation mechanisms of an ECAP-processed LPBF AlSi10Mg alloy in order to correlate them with the macroscopic behaviour reported in a previous article [32]. Consequently, this work focuses on two aspects: first, the effect of ECAP on the microstructure of LPBF AlSi10Mg alloy; second, the evaluation of the deformation mechanisms based on light, electron backscatter diffraction (EBSD) and transmission electron microscopy (TEM) studies.

The novelty of this work lies in the detailed experimental observations and the identification of the active deformation mechanisms acting during severe plastic deformation of the LPBF-AlSi10Mg alloy. It is also shown for the first time that under SPD conditions a novel amorphization transition process begins with preferential phase transitions at some local sites. The results presented in this research article provide valuable information that can be used to improve the overall mechanical properties of additively manufactured Al-Si alloys, and this knowledge provides a general theoretical background for the development of advanced metallic materials and novel post-processing processes.

2. Methodology

2.1. Sample fabrication

The AlSi10Mg alloy samples were obtained by LPBF method on The TruPrint 1000 system using a spherical shape powder supplied by Sigma Aldrich (Fig. 1) and the process parameters given in Table 1. Before running a SLM process powder was sieved with a mesh size of 63 – 80 µm in order to separate oversized particles.

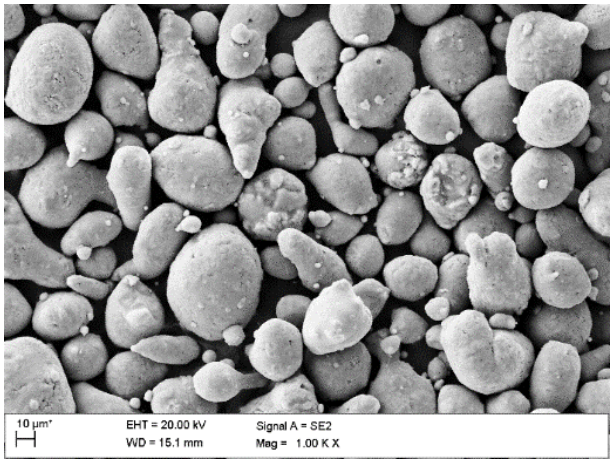

Fig. 1. SEM image of AlSi10Mg powder

Table 1. LPBF process parameters

Scan speed [mm/s]	1400
Laser power [W]	175
Layer thickness [µm]	20
Hatch distance [µm]	90
Protective atmosphere	Argon

Samples of AlSi10Mg alloy obtained by LPBF method were used for the research. Figure 2 shows the external appearances of the sample prior to and after ECAP process.

Fig. 2. Illustration of the test samples – LPBF fabricated (left) and ECAP processed (right)

The specimens obtained by LPBF exhibited low technological plasticity, which made ECAP processing at room temperature difficult; therefore, they were first post-processed according to the following heat treatment scheme:

- Low temperature annealing for 9 minutes at 280 °C. The aim of this treatment was to partially eliminate residual stresses and increase technological plasticity. This type of heat treatment also allowed the partial preservation of the unique heterogeneous cellular microstructure.

2.2. ECAP process

The LabTest 5.2000CT hydraulic press (max. ram speed 400 mm/min) was used for the ECAP experiment. In this configuration the ram speed of the hydraulic cylinder of the press was controlled by oil pressure with the help of a servo valve and an electric motor. Heating was controlled by a dTRON 304 device equipped with a NiCr-Ni thermocouple that could be used up to a maximum temperature of 1350°C. Since the friction effect cannot be neglected in ECAP process, a Nicro-Thermocup 1200 type lubricant was used to reduce the friction coefficient between the ECAP sample and the ECAP die. Subsequently, the specimens (14.25 × 14.25 × 60 mm) were pressed once through a 90° die once at 150 ºC (introducing an equivalent strain of ε = ~1).

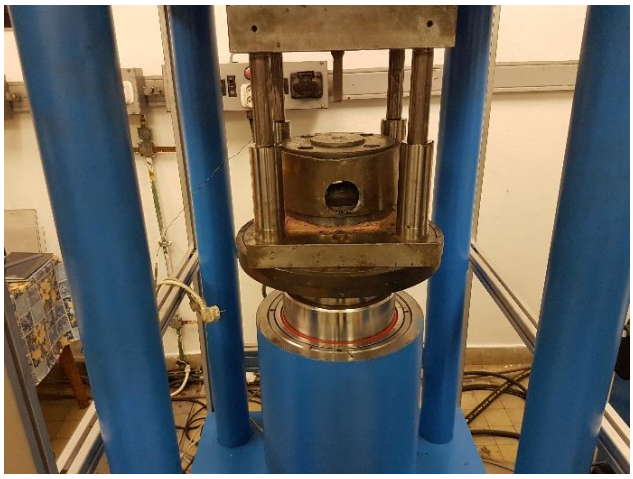

Fig. 3. View of the workstation for material forming using the ECAP process

2.3. Microstructural analysis

SEM and EBSD (electron backscatter diffraction) analyses were performed using a scanning microscope ZEISS Supra 35 operating at an accelerating voltage of 20 kV, a working distance of 17 mm, and a tilt angle of 72°, and using step sizes of 0.12 µm (HT sample) and 0.06 µm (ECAP150 sample). Samples for metallographic and EBSD analyses were prepared in the conventional way - mechanically ground with SiC papers, polished with diamond pastes, and finely polished with 0.04 µm colloidal silica. The averaged KAM values were used to calculate the total geometrically necessary dislocation density (GND) according to methods published elsewhere [42]. For optical metallography, the polished surfaces were etched with Keller's reagent to reveal the details of the microstructure.

X-ray diffraction analysis was performed using a PANalytical X'Pert Pro diffraction system (Malvern Panalytical Ltd., Royston, UK) equipped with a CoKα radiation source. To eliminate the error in the experimental X-ray diffraction profiles caused by the device broadening, the full width at half maximum (FWHM) in the peak profile of a fully annealed pure aluminium was used to determine the structural broadening (i.e., the effective FWHM). Phase composition was evaluated from the XRD peaks, and dislocation density was estimated from microstrain (ε) and crystallite size (D) using software based on the Rietveld refinement method.

Then, the total dislocation density, ρ_{XRD}, was estimated using Eq. (1),

$$\rho_{XRD}=(\rho_d \times \rho_s)^{1/2} \quad (1)$$

where ρ_s and ρ_d are the dislocation density due to the size effect and the dislocation density due to lattice strain, respectively.

2.4. Mechanical properties

Hardness measurements (Hv) were taken for over a rectangular pattern of 14 mm x 14 mm dimension (on the cross-sectional planes of the specimens) using a microhardness tester (Future-Tech FM-ARS), applying a load of 300 g for 15 s. Each indentation was made at equal intervals, separating the points at a vertical and horizontal displacement of 0.84 mm.

3. Results

3.1. Microstructure evolution

3.1.1. Microstructural analysis using optical and scanning electron microscopy

HT sample

Figure 4 present the optical microscopic (OM) and the SEM microscopic images of the heat treated (HT) AlSi10Mg sample. The HT sample in the X-Y plane clearly shows discontinuous laser scan tracks with an average width of 90 µm, showing the bidirectional scanning strategy perpendicular to the build direction of the sample [43]. In Fig. 4(a), the borders of the laser scan tracks are more etched and therefore have brighter outlines. The higher-magnification image of scan track boundary region (MPB – melt pool boundary) (Fig. 4(b)) shows three distinct zones formed due to exposure to different temperature gradients during the LPBF process.

(1) Melt pool (MP fine), characterized by a fine cellular microstructure,
(2) Melt pool coarse (MP coarse), where the width of the cells was almost twice as large as in the fine zones,
(3) Heat-affected zone (HAZ) with a width of 2-3 µm, where isolated Si particles were present.

Figure 4(c) shows the SEM micrograph of the MP fine zone in greater detail. It shows a nearly continuous network of eutectic Si phase (Fig. 4(c)). In addition, nanometric point-like Si precipitates can be seen within the confined Si cells, which is typical of stress-relieved LPBF-Al-Si alloys [44] [45].

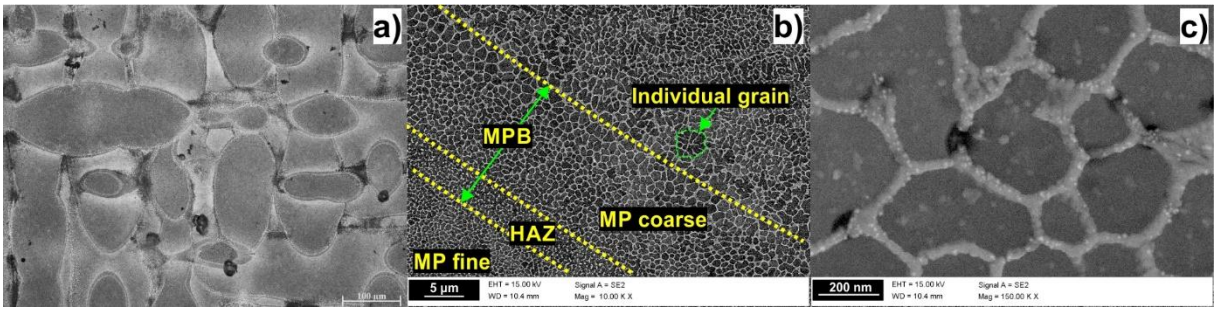

Fig. 4. Microstructure of the heat-treated sample a) OM image, b) SEM image showing the laser scan track border

To obtain a solid understanding of the grain structure, an EBSD analysis was performed. Figure 5(a) shows the inverse pole figure (IPF-Z) obtained from the EBSD with detailed information on grain size and orientation. As can be seen, the building strategy has a significant effect on the grain size distribution. In particular, the sample exhibits a bimodal grain structure characterized by large regions of elongated columnar grains adjacent to the region of fine grains, the melt pool boundary (MPB).

Table 2 shows the microstructural features from the EBSD analysis, where grain boundary angles greater than 2° and less than 15° were considered LAGB and grain boundary angles greater than 15° and less than 63° were considered HAGB. According to these data, about 80% of the grains are considered as grain boundaries with high angle misorientation. On the other hand, about 20% are grain boundaries with low angle misorientation. Such LAGBs in AM-produced metals and alloys are attributed to cellular (equiaxed or columnar) substructure networks formed due to the high cooling rate of the AM process.

Figure 5(b) shows the geometrically necessary dislocation (GND) maps plotted to provide an overview of the density and distribution of dislocations prior to the ECAP process. A maximum dislocation angle of 5° and a Burger vector of 2.86 Å were assumed to generate these maps. As can be seen, the GND networks cluster within larger grains, so it can be concluded that these particular areas are "pre-existing dislocation networks" created by the high temperature gradients of the laser melting process.

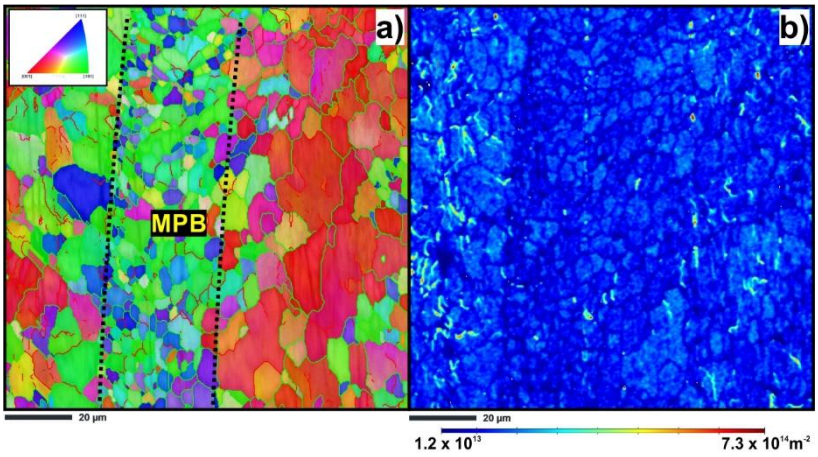

Fig. 5. IPF-Z image (a) with a grain boundary map (HAGBs, with misorientations greater than 15° were marked by green lines, LAGBs, with misorientations 2°<θ<15° were marked by green lines) and (b) GNDs map of heat-treated sample

Table 2. Microstructural parameters of heat treated sampleobtained from EBSD analysis

f_{LAGBs}, %	f_{HAGBs}, %	Grain size, µm
20.1	79.9	3.89

ECAP processed sample

Figure 6 show the optical microscopic and SEM microscopic images of the ECAP150 sample. Metallographic analysis shows that a characteristic microstructure composed of semicircular ("fish scale") patterns has formed. Accordingly, it is clear that the density of the melt pool boundaries (MPB) has increased dramatically. It is also clear that initially continuous Si network is now partially interrupted and coarser (Fig. 6(c)).

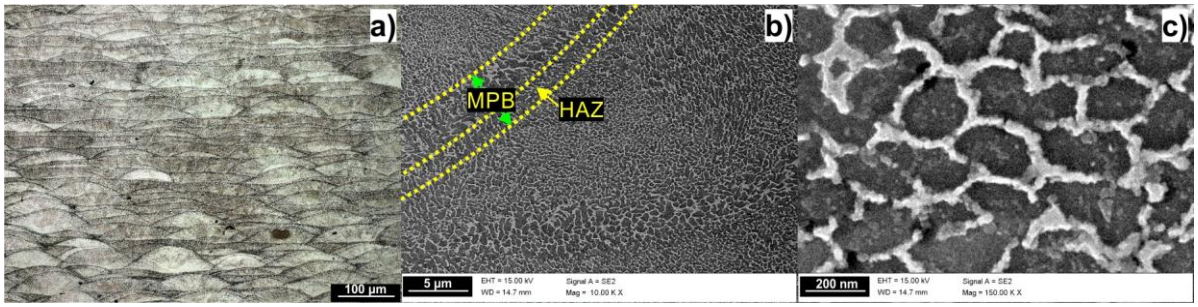

Fig. 6. Microstructure of the ECAP150 sample a) OM image, b) SEM image showing the melt pool boundary region, c) high magnification SEM image showing the cellular structures inside the MP fine zone

Figure 7 shows the EBSD mapping results of ECAP processed sample. In Fig. 7(a), the band contrast (BC) map is shown to highlight the contrast between individual cells (subgrains). In this image, areas with higher lattice distortion have lower pattern quality, which is why they are darker. Comparing this BC map with the SEM micrograph (Fig. 6(c)), it is clear that the black dots in the BC map correspond to Al/Si interfaces, indicating a high dislocation density near these areas.

Figure 7(b) shows the IPF-Z map obtained from EBSD with detailed information on grain size and orientation. As can be seen, the grain size is at least one order of magnitude larger than the cell size. In other words, each grain consists of multiple cells (subgrains). From the statistical data in Table 3, it is clear that severe grain refinement has occurred, as the average grain size has decreased from 3.89 µm to 0.35 µm.

Figure 7(c) shows the grain boundary map. As can be seen about 52% of the grains have high-angle misorientation. This means that the percentage of HAGBs has decreased by 27% after ECAP, indicating the formation of multiple dislocation walls or dynamically recovered small subgrains with a low misorientation angle.

To better understand the heterogeneous deformation of ECAP processed sample, the GND map was plotted. As shown in Fig. 7(d), the GNDs accumulate at the Al/Si interfaces and create stress concentration points (red "hot spots" on the GND map with $\rho_{GND} = 4.6*10^{15}m^{-2}$) whose density and intensity depend on the number of stacked dislocations, confirming that the deformation was heterogeneously distributed between the two phases [46]. Interestingly, there is only a small increase in GND density from $1.22*10^{14}m^{-2}$ to $6.84*10^{14}m^{-2}$, suggesting that the high-density GNDs were rearranged into subgrain structures, i.e., low-angle grain boundaries (LAGB), to reduce the deformation strain distortion energy of the grains [47].

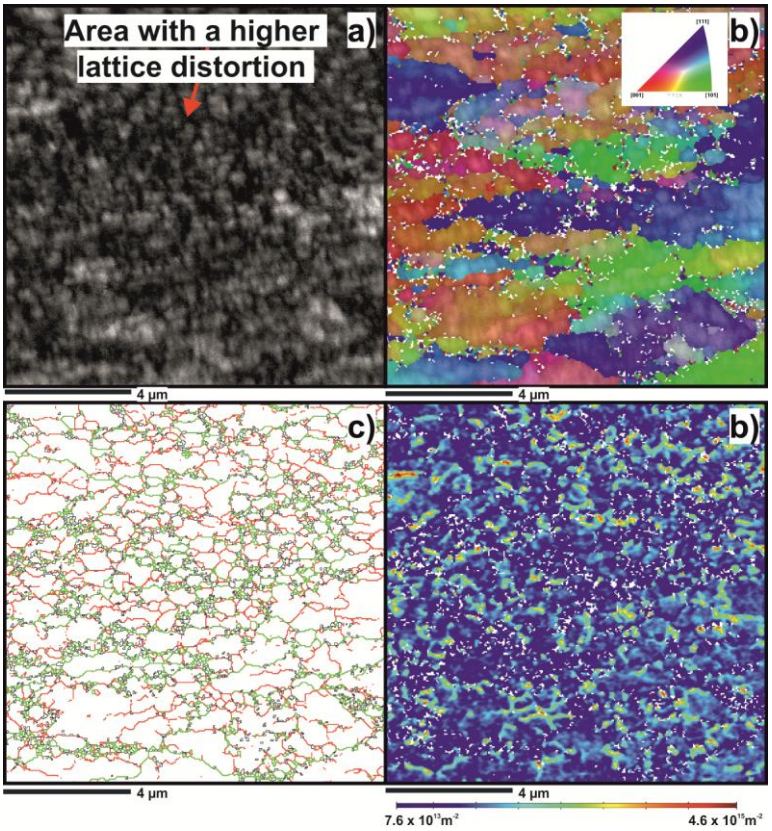

Fig. 7. Results of the EBSD analysis of ECAP150 sample a) band contrast map, b) IPF-Z map, c) grain boundary map (HAGBs, with misorientations greater than 15° were marked by green lines, LAGBs, with misorientations 2°<θ<15° were marked by green lines), d) GNDs map

Table 3 Microstructural parameters of ECAP-processed sample obtained from EBSD analysis

f_{LAGBs}, %	f_{HAGBs}, %	Grain size, µm
47.1	52.9	0.35

To explain the observed microstructural evolution, one must consider the metal flow and theoretical shear patterns in the ECAP process. As the billet passes through the deformation zone in the ECAP die, its front part rotates. Then, as the billet moves through the transition between two die channels, a strong shear (at an angle of 45° to the top and bottom sample surfaces) occurs [48]. This is usually reflected in the formation of a layered (pancaked) grain structure. It is noticeable here that the microstructure evolution of the LPBF sample differs from its conventional counterparts. Here, the ND-TD plane consisted of a series of semicircular (fish scale-like) patterns (typically observed in the X-Z plane of LPBF specimens) instead of a series of discontinuous laser scan traces. This microstructural evolution is the result of the initial rotation of the front part of the billet. The intense shear then changes the shape of the grains; however, in the case of LPBF alloys, it also leads to a reduction in the distance between the HAZ zones. This is because the HAZ zone deforms more than the interior of the melt pool during ECAP processing, because the Si particles in the heat-affected zones (HAZ) are spherical, which contributes to a lower macro yield point of the HAZ due to a weak load transfer effect. Therefore, local plastic deformation occurs preferentially in the HAZ [30] [49].

3.1.2. Microstructural analysis using transmission electron microscope

HT Sample

Next, to examine the microstructures of the heat treated and ECAP150 samples in greater detail, TEM analyses were performed. Figure 8 shows bright- and dark-field microstructures along the building direction (X-Z plane). It confirms that the high solidification rate favours the epitaxial growth of columnar grains [50]. Local modulation of the BF contrast of the Al phase indicate that the grains are composed of multiple sub-micrometer Al cells (see red dotted line in Fig. 6(a)). A unique feature observed in some grains is the intricate network of dislocations, Figs. 6(c) and (d). Several factors can cause the formation of dislocations in LPBF components. For example, dislocations can form when growing dendrites collide during rapid solidification at a cooling rate of ~10^5-10^6 K/s. Furthermore, a thermal mismatch between the Al matrix and precipitates usually leads to the formation of dislocations during the cooling process [51].

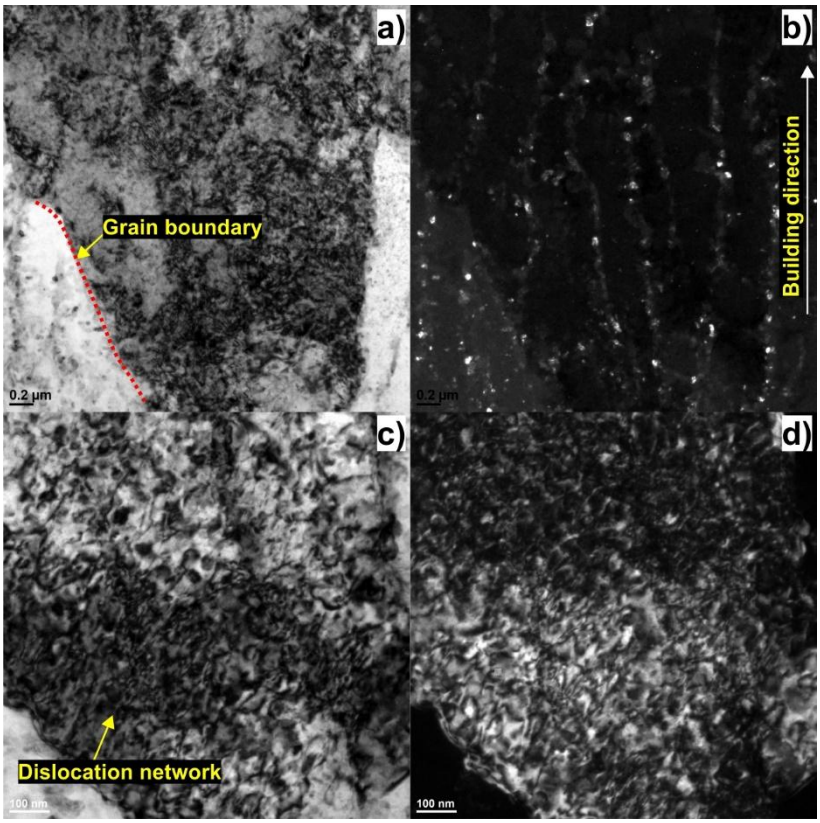

Fig. 8. Representative TEM images of heat-treated sample showing a high density area a) and c) Bright-field TEM b)and d) dark-field TEM images

ECAP processed sample

Figure 9(a) shows the low-magnification bright-field TEM image of the ECAP150 sample. As seen, extreme shear stresses during the ECAP process led to an additional increase in dislocation density, indicating that the deformation of the aluminium phase is mainly controlled by dislocation slip. The bright- and dark-field TEM micrographs taken at higher magnification (Fig. 9(b)-(c)) and the high-resolution TEM images (Fig. 9(d)-(e)) show more details of the substructure of the ECAP150 sample. It is visible that the accumulation led to the formation of subgrains separated by boundaries with low angles of misorientation. Therefore, it can be concluded that the process of grain refinement of the α-Al phase occurred through the transformation of high-density dislocations into subgrain boundaries.

The HRTEM image of the boundary region (highlighted in Fig. 9(c) – see yellow square) confirms the presence of LAGBs, as the misorientation angle between two grains is about 4.7º. It is noticeable here that this subgrain boundary was formed by localized slip of the screw dislocation. In aluminium alloys, screw dislocations can slide crosswise (since aluminium has a high stacking fault energy), which allows faster dynamic recovery to compensate for strain hardening during ECAP deformation. According to Al-Fadhalah et al. [52] this leads to a faster evolution of the UFG equilibrium structure and eventually to saturation in terms of strength and hardness.

Fig. 9(d) shows the existence of twin bands within the Si precipitates. Interestingly, the Fast Fourier transform pattern (with polycrystalline rings) of a boundary region (highlighted in Fig. 9(b)) also shows the absence of a periodic structure, indicating a possible deformation-induced amorphisation of the silicon phase in the solid state [53].

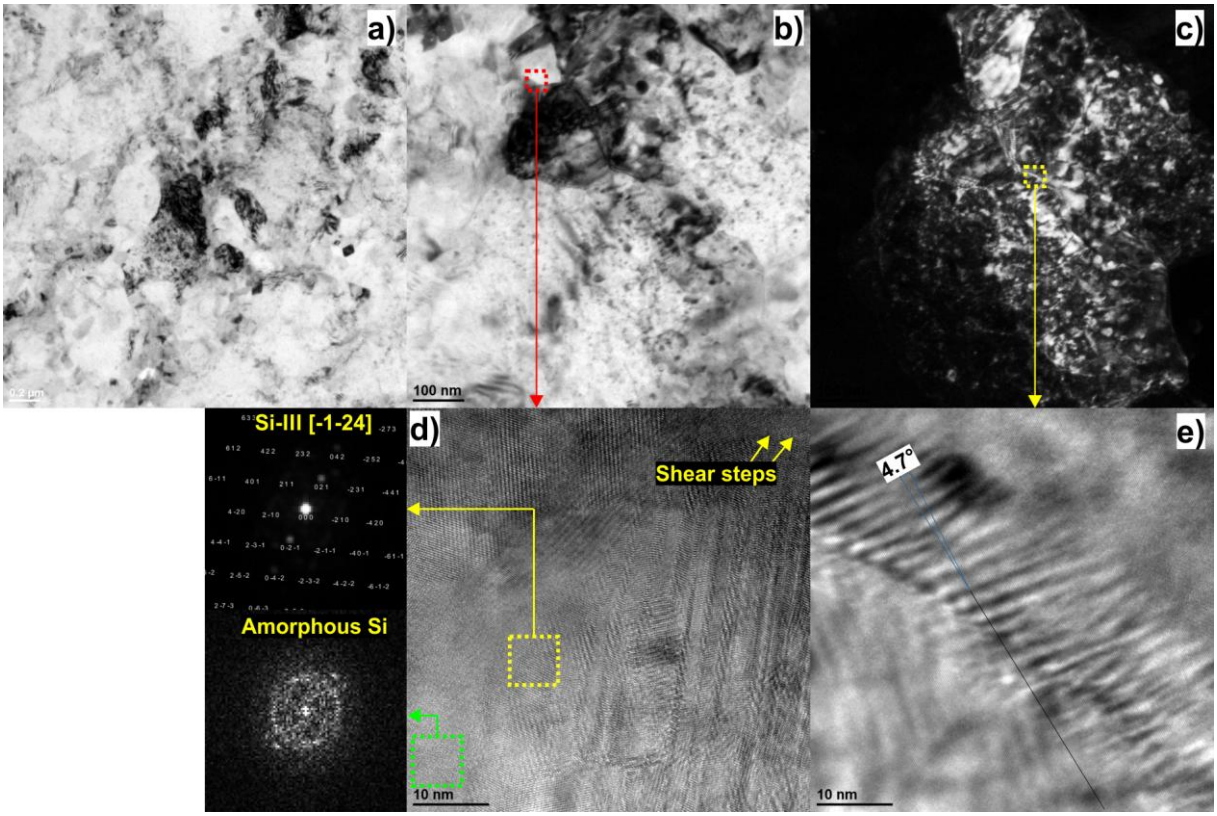

Fig. 9. TEM images of ECAP150 sample a) low-magnification image showing a general microstructure, b) and c) higher magnification brightfield and darkfield TEM images, d) and e) HRTEM images showing the boundary regions highlighted in Figs. 9(b) and (c), respectively.

The HAADF image and the EDS maps registered near the eutectic region (Fig. 10(a)) clearly confirm that, in addition to the aluminium phase, the Si particles were refined down to about 100 nm (brighter areas in Fig. 10(a) are enriched in higher atomic number elements). According to the EDS element mapping analysis shown in Fig. 10(b)-(d), Mg is uniformly distributed in the aluminium matrix, while Si particles with sharp, are preferentially found at the cell boundaries. In addition, several Si rich clusters/nanoparticles (~20 nm in size) are seen within the cells, confirming intense particle refinement/distribution after ECAP processing.

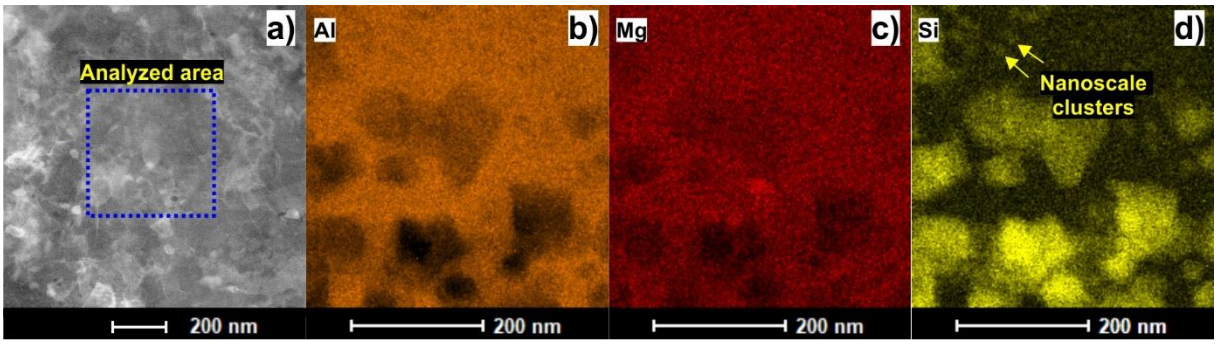

Fig. 10. HAADF image (a) and distributions of (b) Al, (c) Mg, (d) Si observed by EDX mapping

Examination in HRTEM mode of the Al/Si boundary region (Fig. 11) reveals that multiple stacking faults (SFs) and secondary twins forms within another Si nanograin. The measured planar spacing of 0.313 nm (Fig. 10(a)) corresponds to the cubic Si-I phase [54]. The Fast Fourier Transform (FFT) pattern extracted from the interface shows diffuse halo rings, confirming that amorphous structures exists near the Si-rich eutectics. The HRTEM image of the magnified region (marked by the yellow square in Fig. 10(a)) shows the interior of the Si nanograin with twin bands coherently tilted by 141 °; see Fig. 10(b). According to [35], these types of deformation twins in nanocrystalline materials (with a 141° grain boundary) arise from the multiplication of partials with the same Burgers vector.

Interestingly, in the next image taken with the STEM detectors, another polymorphic Si phase was identified - bcc Si-III (Fig. 10(c)). Here, even more intense interactions between twin bands and SFs can be seen (see white arrows). According to Kivambe et al. [55], these SFs and deformation twins within the Si nanograins should have profound effects on the strength and toughness of the studied alloy. SFs may not only act as strong barriers to dislocation glide in a similar way to grain boundaries and impurities, but also actively participate in dislocation generation. The formation of deformation twins can also contribute to plasticity, so that twin bands can play a crucial role in accommodating the dislocations. A higher magnification of the area where the twin bands intersect (marked by the red square) in Fig. 11(c) reveals the presence of Lomer-Cottrell locks (L-C), represented by the pentagon with five red dots at its corners, Fig. 11(e). The second inset (indicated by the green square in Fig. 11(c)) confirms that the formation of twin bands was accompanied by the presence of partial dislocations (indicated by the blue "L"). Such partial dislocations can resolve the local stress concentration leading to twinning or detwinning [56]. It can be speculated that these structural defects - stacking faults, deformation twins, and Lomer-Cottrell locks - were induced by ECAP shear deformation and synergistically strengthened the hard Si phase, increasing the overall strength of the AlSi10Mg alloy.

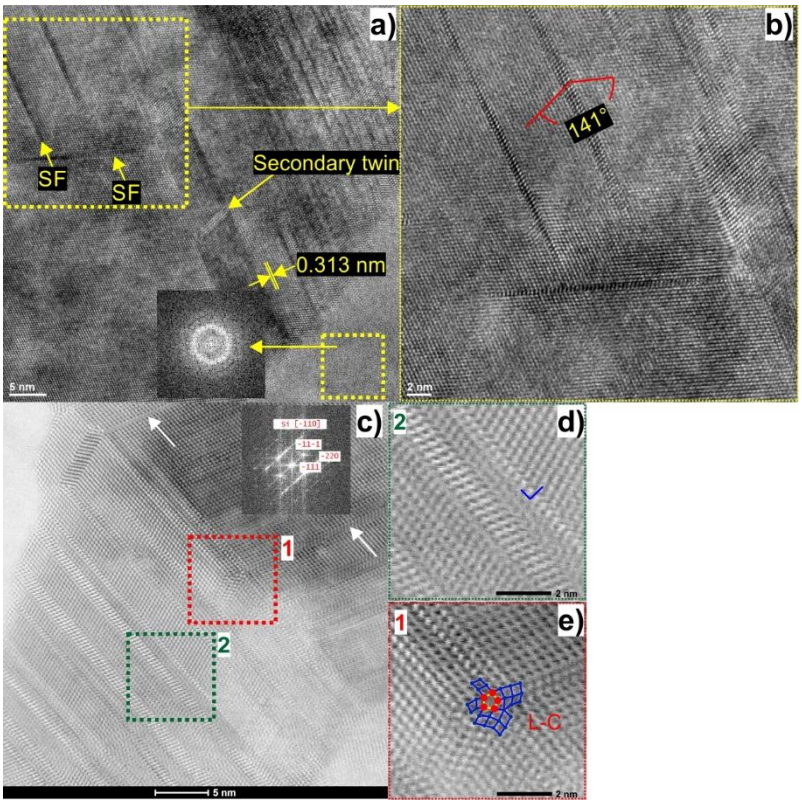

Fig. 11. The TEM images of ECAP150 sample a) and b) HRTEM images of the nanocrystalline Si phase, c), d) and e) STEM images showing highly twinned/faulted Si precipitate

3.2. XRD and average dislocation density

Fig. 12 shows the diffraction patterns obtained by XRD scanning of AlSi10Mg alloy samples. The main reflections corresponding to the two crystalline phases of aluminium and silicon (Si-I phase) can be seen. The inset in Fig. 12 shows broadened and shifted Al(111) peaks in the XRD patterns of the ECAP-processed sample, which is a common observation for SPD-processed nanostructured metals. The peak shift and broadening are caused by lattice defects, such as internal microstrains, dislocations, small crystallite sizes, and additional grain boundaries.

To better understand the evolution of the microstructure after ECAP processing, the XRD measurements are combined with Rietveld analysis (see Table 4). It can be seen that the ρ_{XRD} values are on the order of 1×10^{14} m^{-2}, much higher than $\times 10^{9}$ or $\times 10^{10}$ m^{-2} for conventional cast or wrought metals. Such high ρ_{XRD} values for the as-built sample can be attributed to the presence of pre-existing dislocation networks. The dislocation density in the AlSi10Mg alloy decreased after heat treatment, indicating a partial release of residual stresses. In this condition, the dislocation density was comparable to the value of dislocation density of a similar cast alloy [57]. It is also confirmed that the dislocation density increased to 2.95×10^{14} m^{-2} after ECAP treatment.

It is also noticeable that the Si peaks of the built and heat-treated samples are less intense than those of the ECAP150 sample, which could be related to the precipitation of excess Si from the supersaturated aluminium matrix. The Si peaks in the diffraction pattern of the ECAP150 sample are also broader (even compared to those of the Al phase), indicating the strong refinement of the Si crystallites, which is consistent with the TEM results presented above [58].

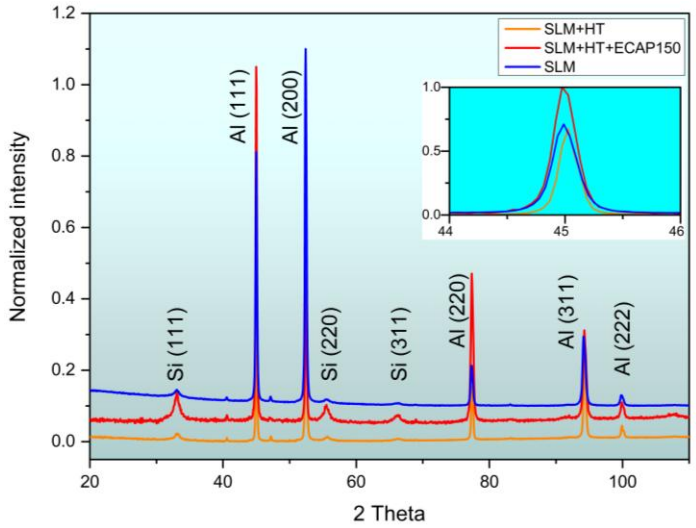

Fig. 12. XRD diffraction pattern of the AlSi10Mg alloy in different conditions

Table 4. Evolution of microstructural parameters from XRD analysis

	LPBF (SLM)	HT	ECAP150
Lattice parameter, Å	4.0495	4.0470	4.0494
Dislocation density (ρ_{XRD}), (m^{-2})	1.55×10^{14}	6.07×10^{13}	2.95×10^{14}

3.3. Hardness evolution

Figure 13 presents the results of the Vickers microhardness measurements on the cross sections of the samples in a form of colour contour maps, in which the HV values are indicated in the colour key to the right of the hardness maps. As can be seen, Fig. 13(a) ,the as-build sample has a relatively homogeneous hardness distribution with an average value of 142HV. From Fig. 13(b) it is clear that the heat treatment results in a decrease of the HV value to 138HV, which can be attributed to the coarsening of the cellular Si network and residual stress removal. The microhardness increases inhomogeneously after the ECAP process with noticeably higher values around the top and bottom regions compared to a central region of the billet, Fig. 13(c). The average measured HV value of the ECAP150 sample is 153HV.

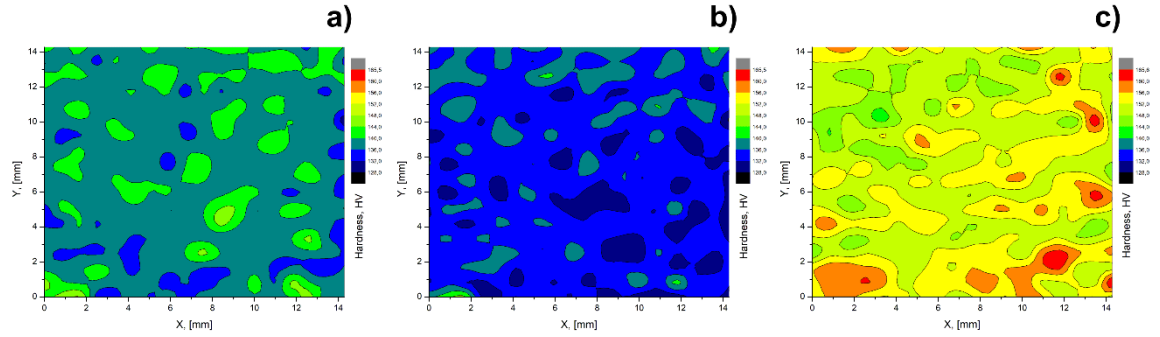

Fig. 13. Vickers microhardness color-coded distribution maps over the cross sections of a) as-built, b) heat-treated, c) ECAP150 sample (dark blue “cool spots” correspond to the hardness value of ~132 HV while red “hot spots” to the hardness value of ~165 HV)

4. Discussion on deformation mechanisms

4.1. Dislocation slip

In materials with face-centred cubic crystal structure (FCC), plastic deformation is caused by dislocation slip, in particular by the octahedral {1 1 1} < 1 1 0 > slip systems [59]. The detailed microstructural analyses presented in this article confirmed massive dislocation activity and its additional accumulation. However, it should be noted here that the increase in hardness reported in an earlier subsection (as well as the increase in yield strength reported in an earlier article [32]) can only be partially attributed to these dislocation activities, as other strengthening mechanisms responsible for the increase in hardness. Figure 14(a) shows a STEM image taken at low magnification in which multiple subgrain with a sizes of about 300 nm can be seen. The appearance of dislocation loops in Fig. 14(b) shows that the dislocation slip is not continuous, which can be explained by the Frank-Read dislocation multiplication mechanism [60]. Careful analysis of this image suggests that multiple mobile dislocations accumulated within the α-Al subgrains during the ECAP process and that these dislocations interacted locally with fine precipitates (see yellow arrows) and/or solute atoms. It can also be assumed that the ECAP processing led to an expansion of the solubility of silicon in the aluminium matrix [28], and therefore these solute atoms could also trigger a strong drag effect in the dislocation field and block mobile dislocations during deformation. At this point, it should be mentioned that solute atoms in the α-Al matrix also play a role in solid solution strengthening and may contribute to the anomalous strain hardening [61]. It also appears that in addition to the Si precipitates, the eutectic Si network acted as favourable sites for the entanglement of mobile dislocations and the formation of accumulated dislocation networks, and together with the pre-existing dislocation network structures, contributed to an increase in SSD density of 2.95×10^{14} m^{-1} [62] [63].

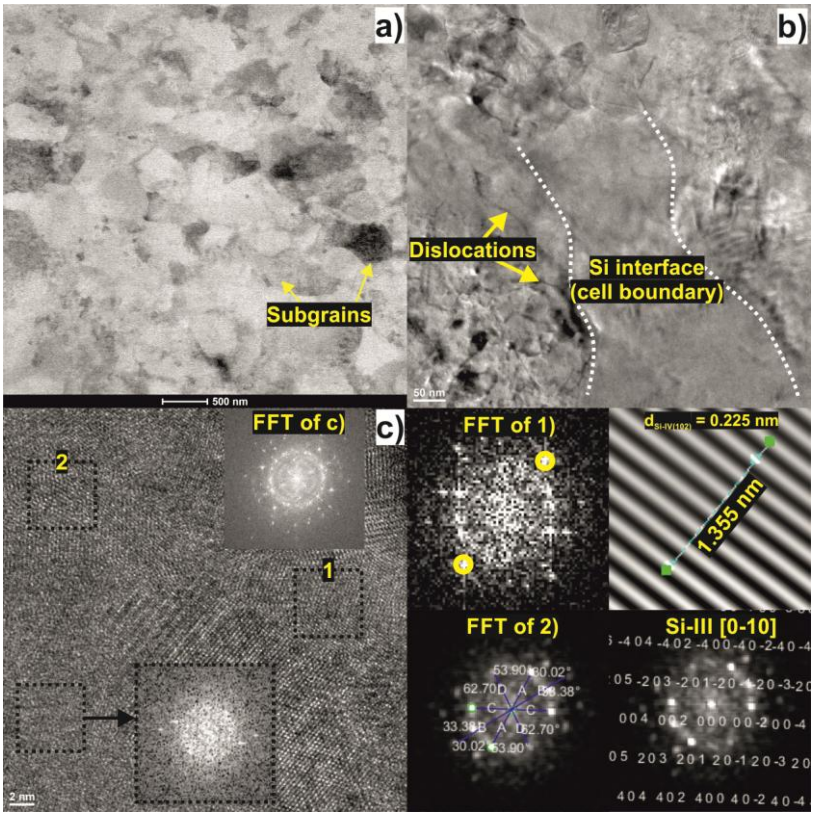

Fig. 14. TEM images showing the microstructure of ECAP150 sample, a) STEM micrograph, b) TEM micrograph of the Al/Si boundary area, c) HRTEM image showing amorphous nanodomains located at the Si phases boundaries (The FFT pattern in (c) indicates that these nanograins have random crystallographic orientations and consist of Si-III phase).

The observed strong grain refinement can be attributed to the simple shear deformation in the ECAP process, which leads to a particularly high slip concentration in a {111} plane. In the investigated SLM-AlSi10Mg alloy, the Al/Si interfaces as well as the pre-existing dislocation networks blocked the dislocation slip, leading to a very rapid accumulation of SSDs and GNDs especially around these interfaces [64], which accelerated the refinement of cell blocks (after the ECAP process, new subgrains are formed at pre-existing grain boundaries; therefore, it can be assumed that one Si cell corresponds to one subgrain), which led to the formation of dynamically recovered subgrains [65] with low misorientation angles. This indicates that this post-mortem TEM study shows an early stage of the grain refinement process - it is not yet a fully developed nanocrystalline structure [66]; however, some DRX grains have formed in the microstructure, Fig. 15. It is worth noting that this observation is consistent with the data in this reference [28]. In this article, it is shown that these LAGBs transform into HAGBs with increasing strain accumulation, leading to the formation of refined polygonalized grains by dynamic recrystallization (DRX).

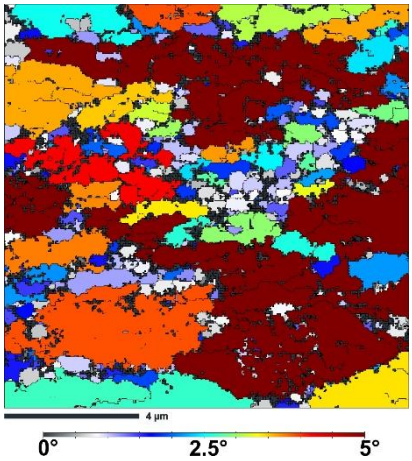

Fig. 15. GOS map of ECAP150 sample. GOS represents the average deviation between the orientation of each point in a given grain and the average orientation of that grain. The grain with threshold degree of GOS≤2° can be defined as recrystallized grain.

4.2. Mechanical twinning

In Al-Si alloys, the twinning of the Si phase can be caused by several mechanisms. The first mechanism, which is frequently described in the literature, is the phenomenon of impurity-induced twinning (IIT) [67] [68]. In this case, the twins are formed in the Si precipitate by absorption of the atoms of the modifier at the growth stages of the solid-liquid interface [69]. The second mechanism is the formation of nantowins during the precipitation treatment. According to the work of Liu et al. [70], multiple nantowins can form on the eutectic Si as a result of the rapid precipitation of Si atoms during annealing. However, such twins can be easily distinguished because the formation of the annealing twin is always accompanied by recrystallization and at least one side of the annealing twin is connected to the grain boundary [71]. The third mechanism of twinning is related to large undercooling at the Al/Si interface and segregation of dissolved Mg due to rapid solidification. However, the resulting crystal defects in the eutectic Si all disappear due to diffusion, accumulation and rearrangement of Si atoms during heat treatment [72]. The last commonly described mechanism is the formation of mechanical twins after tensile deformation or extreme shear deformation. It is believed that deformation twins can contribute significantly to the plastic deformation of Al-Si alloys

and therefore play an essential role in maintaining a uniform strain hardening condition and increasing strength and ductility [73].

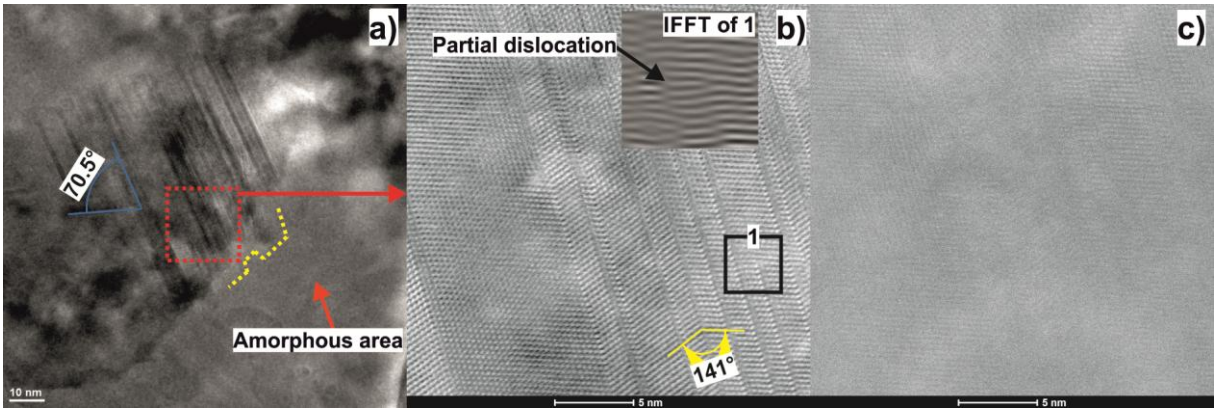

Fig. 16. Results of TEM observation of twinned Si-I precipitate, a) low magnification TEM image showing stacking faults, twins, and secondary twins formed in the precipitate (note that this is the same Si-I precipitate as in Fig. 11(a)), b) HR-STEM image of the boundary region marked by a red square in (a) showing twin bands, stacking faults, and partial dislocation, c) HAADF-STEM image of (b)

Based on the TEM study, Fig. 16, the IIT mechanism can be excluded, as there is no evident element segregation within the twin bands (it is expected that in case of segregation of heavy elements at the twin boundaries, it would appear with a much brighter contrast in the HAADF-STEM image, since the intensity of the atomic columns in a HAADF image is approximately proportional to the square of the atomic number).

An indication that the observed twins were formed by plastic deformation is the fact that annealing twins occur without grain shape. This means that conventional deformation twinning usually generates macroscopic strains and change the grain shape. As shown in Fig. 16(a) the grain boundary segments are not smooth at locations where they intersect the twin boundaries (see yellow dashed lines highlighting the characteristic steps caused by shear deformation).

The post-mortem HRTEM observations and the analysis of the literature allow to justify the mechanical twinning of Si precipitates using strain gradient theory [74]. Due to the pre-existing microstructural heterogeneity of the LPBF-AlSi10Mg alloy (soft aluminium matrix/hard Si cell boundaries), geometrically necessary dislocations (GNDs) were generated near the heterointerfaces (Al/Si interfaces) during severe plastic deformation to support compatible deformation [75]. The deformation incompatibility between the two phases resulted in load transfer from the plastically deformed α-Al matrix to the hard Si phase. As long as the load transfer occurred, the stresses between the phases also increased. When the local stress concentration exceeded the critical shear strength of Si (approx. 10 GPa), twin deformation occurred within the Si particles, resulting in continuous deformation from the relatively ductile α-Al matrix to the brittle eutectic Si phase [76].

In Figure 7(d) it was found that cell boundaries act as heterogeneous sites for the increase in GNDs. In his image, "hot spot" areas represent sites of increased shear localization and stress accumulation, supporting the hypothesis of stress-induced mechanical twinning. Moreover, it appears that these twins were formed by simultaneous and cooperative activation of different Shockley dislocations on symmetric {111} slip planes [77] [78], which is a preferred deformation mode in nanocrystalline materials. The intersection angle between the two atomic layers thick stacking fault and a twin band strictly follows the theoretical angle of 70.5º due to the formation of partial dislocations [79], which supports this hypothesis, Fig. 16(a).

The STEM image (Fig. 16(b)) confirms that the partial dislocations originated at the crystal boundary and formed a stacking fault behind. It can therefore be assumed that the emission process is accompanied by the generation of partial Shockley dislocations. One partial dislocation is immobile (located at the interface) while the other partial dislocation moves within the crystal. The mobile partial dislocation slides along a crystallographic plane and a stacking fault is formed [80] [81] [82]. Further growth of the twin lamella obviously requires increased stress concentration; However, when such conditions are met, a stacking fault consisting of few partial dislocations (few atomic layers) is generated, and this stacking fault turns into a twin band with a thickness of at least three atomic layers [83].

Interestingly, it was also observed that the partial dislocations were emitted from an amorphous crystalline interface, which according to this study [84] could also be sources emitting partial dislocations. This casts doubt on the possibility of a dislocation pileup induced phase transformation of the Si phase, which is detailed in the next subsection. According to Chen et al. [85], the stress concentration can be relieved not only by phase transformations but also by dislocation propagation, cross slip and twin nucleation. Therefore, it seems that we are dealing here with a mixed deformation mode that includes phase transformation, amorphization and mechanical twinning, the latter being the dominant deformation mode of Si at temperatures in the range of 150–200 °C [86].

4.3. Solid state amorphisation

Amorphisation is proposed as a deformation mechanism that contributes to the release of applied strain energy [87]. In general, under extreme shear conditions (e.g., severe plastic deformation), solid state amorphization can occur [88]. Nevertheless, there is limited information in the literature about the presence of amorphous phases in the LPBF-Al-Si alloy system [89]. For example, very rapid local cooling rates during the atomization process can lead to the amorphization of microstructure components (e.g., the eutectic silicon phase), which becomes "frozen" in an amorphous or disordered crystalline phase [90]. Similar to the surface laser processing of Al-Si alloys [91], the formation of the amorphous Si phase in the LPBF-AlSi10Mg alloy was also recently attributed to the short existing time of the melt pool (rapid cooling enables transformation of crystalline silicon phase to the amorphous state) [92]. However, there is no information in the literature about deformation induced solid state amorphization (SSA) in LPBF-Al-Si alloys.

Fortunately, the transition from crystalline to amorphous state by application of pressure (and/or shear) has been extensively studied in the last decades; therefore, there are several molecular dynamics simulations (MD) and experimental studies confirming the deformation-induced transition from crystalline to amorphous state of silicon phase [53] [93] [94] [95] [96] [97]. Most of the aforementioned studies suggest that solid-state amorphization (SSA) is caused by twin/stacking faults, which play the role of nucleation sites. The collapse of crystalline structure may also be related to the accumulation of dislocations, a substantial increase in the density of linear and point defects at the boundaries [98] as high lattice disorder has been observed in areas with high dislocation density [99]. Deformation-induced dislocations with high-energy configurations tend to relax by upsetting more lattice sites near the amorphous regions. Alternatively, the amorphous phase may arise from the dislocation core regions by absorbing more dislocations to reduce the energy of the system.

Amorphisation in the solid state can also occur when the phase free energy is above the critical level [100]. According to the study by Shen et al [101], such transformation is possible when a suitably small "critical" grain size (estimated to be in the range of ~3 nm to ~8 nm) is reached so that the free energy of amorphous Si is attained. Such grain sizes can obviously be achieved by SPD

processing. It has also been found that extremely rapid unloading can lead to direct amorphization of Si phase, while the slow unloading rate leads to the formation of other crystalline phases such as Si-XII, Si- III, Si- IV, Si- III [102] [103]. It has also been reported that the combined effect of rapid solidification, SPD processing by high pressure torsion (HPT) and subsequent annealing can lead to the formation of homogeneous nanostructured states with different grain sizes (10-200 nm) [104] or "amorphous nanoclusters". Therefore, to clarify whether the readily observed amorphisation of the Si phase is due to SSA, several Si precipitates from different ECAP150 sample regions were analysed by HRTEM in this article (see Figs. 9 and 11). At this point, it should be emphasised that the tendency to solid state amporphisation under severe plastic deformation is not the same as the tendency of alloys to amorphise under rapid crystallisation conditions (these are controlled by different physical parameters) [105]; therefore, each of the above mechanisms is analysed with special attention in this subsection.

The first mechanism considered here, which allows the formation of the amorphous Si phase, is the liquid-amorphous transition. Obviously, the cooling rate in selective laser melting is high enough to cause the direct formation of an amorphous Si phase. However, according to the in-situ tensile tests presented in this article [90], the disordered Si phase in the LPBF-AlSi10Mg alloy tends to crystallise during heat treatment at temperatures above 160 °C. On the other hand, it was found in this work [106] that complete nanocrystallisation of the Si network can be achieved only by reheating at 350 °C. Based on the literature data [90] [106], and considering the post-processing history of the AlSi10Mg alloy sample (heat treatment at 280 °C followed by 1 ECAP pass at 150 °C), it can be speculated that the high cooling rates during gas atomization or selective laser melting may have created favourable conditions for the formation of amorphous grain bodies around the Si precipitates.

The second mechanism which allows the formation of the amorphous Si phase, is related to twin/stacking faults or the collapse of the crystalline structure due to the accumulation of dislocations. In contrast to previous findings [94], the TEM investigation results presented in this article did not provide experimental evidence for amorphisation of the Si phase induced by twin interactions. However, since the dislocation motion was strongly hindered due to numerous interfaces such as grain boundaries or cell boundaries, the high dislocation accumulation near these interfaces could lead to the formation of amorphous regions in the ECAP150 sample. According to the work of Li et al. [107], islands of amorphous material form when the defect density in the Si precipitates reaches a critical level, creating favourable conditions for solid state amorphisation.

Although it is difficult at this stage to determine whether the amorphous regions observed by HRTEM are due to SSA or the result of melting and quenching, the presence of shear stress during the ECAP process can undoubtedly lead to pressure-induced amorphisation and polymorphism; therefore, the third mechanism considered here is the localized solid-state amorphisation under the extreme deformation conditions.

Interestingly, the HRTEM analysis described in an earlier section shows the presence of two distinct Si phases, fcc Si-I (a common observation in LPBF Al-Si alloys) and bcc Si-III (not previously reported in LPBF Al-Si alloys). This raises the following question: What are the mechanisms responsible for the formation of the bcc-Si- III phase? In this study [108], it is well documented that high stresses (9 - 16 GPa) can lead to the transformation of Si-I into the Si-II phase, which then undergoes further transformation into Si- III upon unloading. This raises another question, "Is it possible to induce sufficiently high phase stresses to trigger the Si phase transformation?" Obviously, the Al and Si phases in the studied AlSi10Mg alloy have different yield strengths and strain hardening

rates; therefore, the stress of the Si phase also changes during plastic deformation due to a load transfer effect. According to these articles [49] [109], the local stress of Si phase increases drastically with increasing strain, up to 8 GPa, which may alternatively lead to its fragmentation. On the other hand, molecular dynamics (MD) shows that the emission of partial dislocations and/or stacking faults requires higher stresses, since silicone behaves elastically up to ∼10 GPa [97]. This suggests that the activation of additional deformation modes (mechanical twinning or stacking fault formation) requires higher phase stresses (above 10 GPa). Therefore, it can be surmised that the local phase stresses were indeed high enough (in the range of 9 - 16 GPa) to cause the transformation of fcc Si-I into βSn Si-II, which then transformed into bcc Si-III after ECAP processing (upon unloading).

The mechanism of the above mentioned Si phase transformation in the LPBF AlSi10Mg alloy can be described as follows. During the ECAP process, high stresses build up near the Si phase due to the incompatible deformation, inducing the phase transformation from fcc Si-I to βSn Si-II (which is associated with a volume decrease of 22% compared to the Si-I phase). Since the Si-II phase is unstable, it transforms into the Si-III phase [110] immediately when the stress is relieved (after plastic deformation), which is associated with an increase in volume (the Si-III phase has a larger structural volume than Si- II). This transformation causes a kind of "explosion" leading to refinement of the Si phase [101]. Indeed, the XRD data presented above indicate a strong refinement of the Si phase. Moreover, a post-mortem HRTEM analysis of the eutectic region (Fig. 14(c)) documented the apparent fragmentation of the bcc Si-III phase. This HRTEM image also shows several amorphous nanodomains located exactly at the boundaries of the Si crystallites, supporting the hypothesis of deformation-induced solid-state amorphisation at the grain boundaries. It seems that either the high defect concentration or the dislocation activities play an important role in triggering the localized SSA at defect sites [111]. These results also support the hypothesis that the nanocrystalline structure could promote the amorphisation of the silicon phase in the LPBF AlSi10Mg alloy.

4.4. Incompatible deformation – plastic strain gradient

Incompatible deformation between different microstructural constituents (phases/grains) is another important mesoscale deformation mechanism. In general, LPBF-AlSi10Mg alloy exhibits anisotropic mechanical properties, which according to these studies [112] [112] [113] is caused by the heterogeneous nature of the microstructure, as the edge of the molten pool has lower strength than the interior, as shown by nanoindentation tests [114] [115]. Such a heterogeneous and anisotropic microstructure leads to higher strain hardening ability of the alloy [116] and induces long-range hetero-deformation-induced (HDI) stresses.

The second source of incompatible deformation is the Al/Si interface (cell boundary). Due to the difference in mechanical strength between the soft α-Al matrix and the hard Si cell walls, which is about 9.45 GPa according to the publication by Chen et al. [117], large strain gradients occur near the domain boundaries during deformation. The inhomogeneous deformation behavior of the Al/Si interface can be divided into three phases. In the first phase, plastic deformation occurs due to dislocation accumulation in the soft Al phase, leading to the formation of statistically stored dislocations (SSDs) within the cells (the soft domains deform first, while the hard domains remain elastic) [118] [119]. To maintain deformation continuity, GNDs are then generated at the domain interfaces in the soft domain. While these GNDs increase the strength of the soft domain, their accumulation at the Al/Si interface leads to forward stresses in the hard domain [120]and causes early plastic deformation of the hard domain, here deformation twins (see above). However, the strain gradient still exists between the domains because the deformation rate is different (the soft

domains deform faster than the hard domains). Therefore, the GNDs evolve continuously until the strength level of the two domains becomes similar. These GNDs significantly impede the dislocation motion and develop long-range back-stresses and contribute to HDI hardening and strain hardening [108].

The EBSD analysis in Fig. 7(d) shows significant GND accumulation near the Si cell boundary. These GNDs are apparently generated to maintain strain continuity and avoid the formation of stress singularities in the interfacial zone [121]. From the comparison of Fig. 7(c) and (d), it can be concluded that the LAGBs have higher GND density than other regions, which confirms that the GNDs are the sub-grain boundaries that will transform into HAGBs with increasing strain accumulation [122]. It is worth noting that the results described in this section are consistent with previous studies [123][124], that showed much higher stress in the Si rich phase and a very high density of geometrically necessary dislocations (GNDs) near the Al/Si interface.

5. Conclusions

In this article, microstructural refinement and deformation mechanisms were studied in detail using optical, scanning electron and transmission electron microscopy. The main results of this research can be summarised as follows:

- It was found that post-processing of LPBF AlSi10Mg using ECAP enables the formation of a novel submicrometer-grained heterogeneous microstructure.
- A remarkable refinement of the microstructure down to the ultrafine grain range was achieved. According to TEM analysis, the microstructure consisted of subgrains with a size of ~300 nm formed from the pre-existing cellular structures
- TEM, the results provided direct experimental evidence that deformation twinning occurs in the Si phase, suggesting that the transfer of dynamic stress and strain from the soft phase to a hard phase forces the cooperative deformation of the soft phase together with the hard phase.
- ECAP leads to deformation-induced amorphisation of the Si phase and phase transformation in the solid state
- The results presented in this article show that the SLM-AlSi10Mg aluminium alloy with submicrometer-grained heterogeneous microstructure exhibits significantly improved hardness and high ductility compared to its SLM counterpart, and that its mechanical properties can be tuned using severe plastic deformation.
- The hardness improvement of the heterogeneous material is related to the high dislocation density, the reduction in grain size, an increase of Si content in the solid solution, the presence of deformation twins, and the hetero-deformation induced strengthening.
- ECAP processing provides a strategy for developing polymorphic LPBF silicon materials by strain engineering.

Founding

The research was funded by the National Science Centre, Poland based on the decision number 2021/43/D/ST8/1946.

References

[1] D. Mayer, T. Bein, H. Buff, B. Götz, O. Schwarzhaupt, D. Spancken, Enhanced lightweight design by composites – Results of the EU project ENLIGHT, J. Reinf. Plast. Compos. (2018).

https://doi.org/10.1177/0731684418762321.
[2] Y. Zou, H. Ding, Y. Zhang, Z. Tang, Microstructural evolution and strain hardening behavior of a novel two-stage warm rolled ultra-high strength medium Mn steel with heterogeneous structures, Int. J. Plast. 151 (2022) 103212. https://doi.org/https://doi.org/10.1016/j.ijplas.2022.103212.
[3] Z. Wang, W. Lu, H. Zhao, C.H. Liebscher, J. He, D. Ponge, D. Raabe, Z. Li, Ultrastrong lightweight compositionally complex steels via dual-nanoprecipitation, Sci. Adv. 6 (2020) eaba9543. https://doi.org/10.1126/sciadv.aba9543.
[4] H. Wu, G. Fan, An overview of tailoring strain delocalization for strength-ductility synergy, Prog. Mater. Sci. 113 (2020) 100675. https://doi.org/10.1016/J.PMATSCI.2020.100675.
[5] P. Wang, Y. Xiang, X. Wang, Z. Liu, S. Qu, Z. Zhuang, New insight for mechanical properties of metals processed by severe plastic deformation, Int. J. Plast. 123 (2019) 22–37. https://doi.org/https://doi.org/10.1016/j.ijplas.2019.05.005.
[6] H. Chen, Z. Chen, G. Ji, S. Zhong, H. Wang, A. Borbély, Y. Ke, Y. Bréchet, Experimental and modelling assessment of ductility in a precipitation hardening AlMgScZr alloy, Int. J. Plast. 139 (2021) 102971. https://doi.org/https://doi.org/10.1016/j.ijplas.2021.102971.
[7] Y. Wei, Y. Li, L. Zhu, Y. Liu, X. Lei, G. Wang, Y. Wu, Z. Mi, J. Liu, H. Wang, H. Gao, Evading the strength-ductility trade-off dilemma in steel through gradient hierarchical nanotwins, Nat. Commun. (2014). https://doi.org/10.1038/ncomms4580.
[8] H. Shi, N. Zong, J. Le, S. Li, G. Huang, J. Li, J. Mao, W. Lu, Strain hardening versus softening: Anisotropic response of strain hardening-softening transition in a polycrystalline zirconium alloy at room temperature from dislocation viewpoint, Mater. Sci. Eng. A. 847 (2022) 143344. https://doi.org/10.1016/J.MSEA.2022.143344.
[9] T.W. Zhang, S.G. Ma, D. Zhao, Y.C. Wu, Y. Zhang, Z.H. Wang, J.W. Qiao, Simultaneous enhancement of strength and ductility in a NiCoCrFe high-entropy alloy upon dynamic tension: Micromechanism and constitutive modeling, Int. J. Plast. 124 (2020) 226–246. https://doi.org/https://doi.org/10.1016/j.ijplas.2019.08.013.
[10] T.-Z. Zhao, Z.-X. Fan, H.-Z. Xie, H.-R. Chen, S.-F. Chen, S.-H. Zhang, A new modeling framework for anisotropic yield strength of Al-Li alloy sheet with inhomogeneous plate-like T1 precipitates, Int. J. Plast. 157 (2022) 103396. https://doi.org/https://doi.org/10.1016/j.ijplas.2022.103396.
[11] J. Fan, X. Ji, L. Fu, J. Wang, S. Ma, Y. Sun, M. Wen, A. Shan, Achieving exceptional strength-ductility synergy in a complex-concentrated alloy via architected heterogeneous grains and nano-sized precipitates, Int. J. Plast. 157 (2022) 103398. https://doi.org/https://doi.org/10.1016/j.ijplas.2022.103398.
[12] C.W. Shao, P. Zhang, Y.K. Zhu, Z.J. Zhang, Y.Z. Tian, Z.F. Zhang, Simultaneous improvement of strength and plasticity: Additional work-hardening from gradient microstructure, Acta Mater. 145 (2018) 413–428. https://doi.org/https://doi.org/10.1016/j.actamat.2017.12.028.
[13] B. Sadeghi, P. Cavaliere, C.I. Pruncu, Architecture dependent strengthening mechanisms in graphene/Al heterogeneous lamellar composites, Mater. Charact. 188 (2022) 111913. https://doi.org/https://doi.org/10.1016/j.matchar.2022.111913.
[14] S. Lu, J. Zhao, M. Huang, Z. Li, G. Kang, X. Zhang, Multiscale discrete dislocation dynamics study of gradient nano-grained materials, Int. J. Plast. 156 (2022) 103356. https://doi.org/https://doi.org/10.1016/j.ijplas.2022.103356.
[15] X. Wu, Y. Zhu, Gradient and lamellar heterostructures for superior mechanical properties, MRS Bull. 46 (2021) 244–249. https://doi.org/10.1557/s43577-021-00056-w.
[16] Z. Wang, X. Lin, N. Kang, Y. Wang, X. Yu, H. Tan, H. Yang, W. Huang, Making selective-laser-melted high-strength Al–Mg–Sc–Zr alloy tough via ultrafine and heterogeneous microstructure, Scr. Mater. 203 (2021) 114052. https://doi.org/10.1016/J.SCRIPTAMAT.2021.114052.
[17] D.D. Ben, Y.R. Ma, H.J. Yang, L.X. Meng, X.H. Shao, H.Q. Liu, S.G. Wang, Q.Q. Duan, Z.F. Zhang, Heterogeneous microstructure and voids dependence of tensile deformation in a selective

laser melted AlSi10Mg alloy, Mater. Sci. Eng. A. (2020) 140109. https://doi.org/https://doi.org/10.1016/j.msea.2020.140109.
[18] H. Yao, Z. Tan, D. He, Z. Zhou, Z. Zhou, Y. Xue, L. Cui, L. Chen, G. Wang, Y. Yang, High strength and ductility AlCrFeNiV high entropy alloy with hierarchically heterogeneous microstructure prepared by selective laser melting, J. Alloys Compd. 813 (2020) 152196. https://doi.org/10.1016/J.JALLCOM.2019.152196.
[19] X. Li, D. Yi, X. Wu, J. Zhang, X. Yang, Z. Zhao, Y. Feng, J. Wang, P. Bai, B. Liu, Y. Liu, Effect of construction angles on microstructure and mechanical properties of AlSi10Mg alloy fabricated by selective laser melting, J. Alloys Compd. 881 (2021) 160459. https://doi.org/https://doi.org/10.1016/j.jallcom.2021.160459.
[20] S.G. Jeong, G.M. Karthik, E.S. Kim, A. Zargaran, S.Y. Ahn, M.J. Sagong, S.H. Kang, J.W. Cho, H.S. Kim, Architectured heterogeneous alloys with selective laser melting, Scr. Mater. 208 (2022) 114332. https://doi.org/10.1016/J.SCRIPTAMAT.2021.114332.
[21] K.S. Al-Rubaie, S. Melotti, A. Rabelo, J.M. Paiva, M.A. Elbestawi, S.C. Veldhuis, Machinability of SLM-produced Ti6Al4V titanium alloy parts, J. Manuf. Process. 57 (2020) 768–786. https://doi.org/10.1016/J.JMAPRO.2020.07.035.
[22] M. Król, P. Snopiński, A. Czech, The phase transitions in selective laser-melted 18-NI (300-grade) maraging steel, J. Therm. Anal. Calorim. 142 (2020). https://doi.org/10.1007/s10973-020-09316-4.
[23] V.P. Sabelkin, G.R. Cobb, T.E. Shelton, M.N. Hartsfield, D.J. Newell, R.P. O'Hara, R.A. Kemnitz, Mitigation of anisotropic fatigue in nickel alloy 718 manufactured via selective laser melting, Mater. Des. 182 (2019) 108095. https://doi.org/10.1016/J.MATDES.2019.108095.
[24] D. Lin, X. Xi, X. Li, J. Hu, L. Xu, Y. Han, Y. Zhang, L. Zhao, High-temperature mechanical properties of FeCoCrNi high-entropy alloys fabricated via selective laser melting, Mater. Sci. Eng. A. 832 (2022) 142354. https://doi.org/https://doi.org/10.1016/j.msea.2021.142354.
[25] P. Snopiński, A. Woźniak, M. Pagáč, Microstructural Evolution, Hardness, and Strengthening Mechanisms in SLM AlSi10Mg Alloy Subjected to Equal-Channel Angular Pressing (ECAP), Materials (Basel). 14 (2021). https://doi.org/10.3390/ma14247598.
[26] C. Böhm, M. Werz, S. Weihe, Practical Approach to Eliminate Solidification Cracks by Supplementing AlMg4.5Mn0.7 with AlSi10Mg Powder in Laser Powder Bed Fusion, Materials (Basel). 15 (2022). https://doi.org/10.3390/ma15020572.
[27] K. Żaba, L. Tuz, P. Noga, S. Rusz, R. Zabystrzan, Effect of Multi-Variant Thermal Treatment on Microstructure Evolution and Mechanical Properties of AlSi10Mg Processed by Direct Metal Laser Sintering and Casting, Materials (Basel). 15 (2022). https://doi.org/10.3390/ma15030974.
[28] P. Snopiński, A. Woźniak, D. Łukowiec, K. Matus, T. Tański, S. Rusz, O. Hilšer, Evolution of Microstructure, Texture and Corrosion Properties of Additively Manufactured AlSi10Mg Alloy Subjected to Equal Channel Angular Pressing (ECAP), Symmetry (Basel). 14 (2022). https://doi.org/10.3390/sym14040674.
[29] V. Romanova, E. Dymnich, R. Balokhonov, M.S. Mohebbi, V. Ploshikhin, Investigation of the inhomogeneous mechanical response at the grain scale for additive AlSi10Mg alloy, Procedia Struct. Integr. 35 (2022) 196–202. https://doi.org/10.1016/J.PROSTR.2021.12.065.
[30] H. Chen, S. Patel, M. Vlasea, Y. Zou, The Role of the Heterogenous Structure on the Mechanical Properties of Additively Manufactured AlSi10Mg Alloys BT - TMS 2022 151st Annual Meeting & Exhibition Supplemental Proceedings, in: Springer International Publishing, Cham, 2022: pp. 1577–1584.
[31] E. Padovano, C. Badini, A. Pantarelli, F. Gili, F. D'Aiuto, A comparative study of the effects of thermal treatments on AlSi10Mg produced by laser powder bed fusion, J. Alloys Compd. 831 (2020) 154822. https://doi.org/10.1016/J.JALLCOM.2020.154822.
[32] P. Snopiński, K. Matus, F. Tatiček, S. Rusz, Overcoming the strength-ductility trade-off in additively manufactured AlSi10Mg alloy by ECAP processing, J. Alloys Compd. 918 (2022) 165817. https://doi.org/10.1016/J.JALLCOM.2022.165817.

[33] B. Chen, S.K. Moon, X. Yao, G. Bi, J. Shen, J. Umeda, K. Kondoh, Strength and strain hardening of a selective laser melted AlSi10Mg alloy, Scr. Mater. (2017). https://doi.org/10.1016/j.scriptamat.2017.07.025.
[34] H.Z. Zhao, Z.S. You, N.R. Tao, L. Lu, Anisotropic strengthening of nanotwin bundles in heterogeneous nanostructured Cu: Effect of deformation compatibility, Acta Mater. 210 (2021) 116830. https://doi.org/https://doi.org/10.1016/j.actamat.2021.116830.
[35] Y.T. Zhu, X.Z. Liao, X.L. Wu, Deformation twinning in nanocrystalline materials, Prog. Mater. Sci. (2012). https://doi.org/10.1016/j.pmatsci.2011.05.001.
[36] B. Wang, H. Liu, Y. Zhang, B. Zhou, L. Deng, C. Wang, J. Chen, Y. Zhang, Effect of grain size on twinning behavior of pure titanium at room temperature, Mater. Sci. Eng. A. 827 (2021) 142060. https://doi.org/10.1016/J.MSEA.2021.142060.
[37] Y.T. Zhu, X.Z. Liao, X.L. Wu, J. Narayan, Grain size effect on deformation twinning and detwinning, J. Mater. Sci. 48 (2013) 4467–4475. https://doi.org/10.1007/s10853-013-7140-0.
[38] A.S. Khan, C.S. Meredith, Thermo-mechanical response of Al 6061 with and without equal channel angular pressing (ECAP), Int. J. Plast. 26 (2010) 189–203. https://doi.org/https://doi.org/10.1016/j.ijplas.2009.07.002.
[39] P. Snopiński, M. Król, M. Pagáč, J. Petrů, J. Hajnyš, T. Mikuszewski, T. Tański, Effects of equal channel angular pressing and heat treatments on the microstructures and mechanical properties of selective laser melted and cast AlSi10Mg alloys, Arch. Civ. Mech. Eng. 21 (2021) 92. https://doi.org/10.1007/s43452-021-00246-y.
[40] Z. Li, Z. Li, Z. Tan, D.B. Xiong, Q. Guo, Stress relaxation and the cellular structure-dependence of plastic deformation in additively manufactured AlSi10Mg alloys, Int. J. Plast. (2020). https://doi.org/10.1016/j.ijplas.2019.12.003.
[41] A. Hadadzadeh, B. Shalchi Amirkhiz, A. Odeshi, J. Li, M. Mohammadi, Role of hierarchical microstructure of additively manufactured AlSi10Mg on dynamic loading behavior, Addit. Manuf. (2019). https://doi.org/10.1016/j.addma.2019.04.012.
[42] Z. Zribi, H.H. Ktari, F. Herbst, V. Optasanu, N. Njah, EBSD, XRD and SRS characterization of a casting Al-7wt%Si alloy processed by equal channel angular extrusion: Dislocation density evaluation, Mater. Charact. (2019). https://doi.org/10.1016/j.matchar.2019.04.044.
[43] N. Nadammal, T. Mishurova, T. Fritsch, I. Serrano-Munoz, A. Kromm, C. Haberland, P.D. Portella, G. Bruno, Critical role of scan strategies on the development of microstructure, texture, and residual stresses during laser powder bed fusion additive manufacturing, Addit. Manuf. 38 (2021) 101792. https://doi.org/10.1016/J.ADDMA.2020.101792.
[44] M. Wang, B. Song, Q. Wei, Y. Zhang, Y. Shi, Effects of annealing on the microstructure and mechanical properties of selective laser melted AlSi7Mg alloy, Mater. Sci. Eng. A. 739 (2019) 463–472. https://doi.org/10.1016/J.MSEA.2018.10.047.
[45] I. Rosenthal, E. Tiferet, M. Ganor, A. Stern, Post-processing of AM-SLM AlSi10Mg specimens: Mechanical properties and fracture behaviour, Ann. “Dunarea Jos” Univ. Galati, Fascicle XII, Weld. Equip. Technol. 26 (2015) 33–38.
[46] J. Li, C. Fang, Y. Liu, Z. Huang, S. Wang, Q. Mao, Y. Li, Deformation mechanisms of 304L stainless steel with heterogeneous lamella structure, Mater. Sci. Eng. A. 742 (2019) 409–413. https://doi.org/https://doi.org/10.1016/j.msea.2018.11.047.
[47] W. Gu, J. Li, Y. Wang, Effect of dislocation structure evolution on low-angle grain boundary formation in 7050 aluminum alloy during aging, Int. J. Miner. Metall. Mater. 22 (2015) 721–728. https://doi.org/10.1007/s12613-015-1127-6.
[48] M. Furukawa, Z. Horita, T.G. Langdon, Factors influencing the shearing patterns in equal-channel angular pressing, Mater. Sci. Eng. A. 332 (2002) 97–109. https://doi.org/10.1016/S0921-5093(01)01716-6.
[49] X.X. Zhang, H. Andrä, Crystal plasticity simulation of the macroscale and microscale stress–strain relations of additively manufactured AlSi10Mg alloy, Comput. Mater. Sci. 200 (2021) 110832. https://doi.org/https://doi.org/10.1016/j.commatsci.2021.110832.
[50] Q. Tan, J. Zhang, N. Mo, Z. Fan, Y. Yin, M. Bermingham, Y. Liu, H. Huang, M.X. Zhang, A novel

method to 3D-print fine-grained AlSi10Mg alloy with isotropic properties via inoculation with LaB6 nanoparticles, Addit. Manuf. 32 (2020) 101034. https://doi.org/10.1016/J.ADDMA.2019.101034.
[51] K.M. Bertsch, G. Meric de Bellefon, B. Kuehl, D.J. Thoma, Origin of dislocation structures in an additively manufactured austenitic stainless steel 316L, Acta Mater. 199 (2020) 19–33. https://doi.org/10.1016/J.ACTAMAT.2020.07.063.
[52] K.J. Al-Fadhalah, M.K. Alyazidi, M. Rafiq, Effect of Microstructure Refinement on Hardness Homogeneity of Aluminum Alloy 1100 Processed by Accumulative Roll Bonding, J. Mater. Eng. Perform. 28 (2019) 4693–4706. https://doi.org/10.1007/s11665-019-04228-3.
[53] Y.-C. Wang, W. Zhang, L.-Y. Wang, Z. Zhuang, E. Ma, J. Li, Z.-W. Shan, In situ TEM study of deformation-induced crystalline-to-amorphous transition in silicon, NPG Asia Mater. 8 (2016) e291–e291. https://doi.org/10.1038/am.2016.92.
[54] S. Bhattacharya, A.R. Riahi, A.T. Alpas, Indentation-induced subsurface damage in silicon particles of Al–Si alloys, Mater. Sci. Eng. A. 527 (2009) 387–396. https://doi.org/10.1016/J.MSEA.2009.08.052.
[55] M.M. Kivambe, T. Ervik, B. Ryningen, G. Stokkan, On the role of stacking faults on dislocation generation and dislocation cluster formation in multicrystalline silicon, J. Appl. Phys. 112 (2012) 103528. https://doi.org/10.1063/1.4767062.
[56] Y. Zhang, P.C. Millett, M. Tonks, B. Biner, Deformation-twin-induced grain boundary failure, Scr. Mater. 66 (2012) 117–120. https://doi.org/https://doi.org/10.1016/j.scriptamat.2011.10.021.
[57] D. Song, G. Wang, Z. Zhou, E.E. Klu, B. Gao, A. Ma, Y. Wu, J. Sun, J. Jiang, X. Ma, Developing a high-strength Al–11Si alloy with improved ductility by combining ECAP and cryorolling, Mater. Sci. Eng. A. (2020). https://doi.org/10.1016/j.msea.2019.138880.
[58] B. Amir, E. Grinberg, Y. Gale, O. Sadot, S. Samuha, Influences of platform heating and post-processing stress relief treatment on the mechanical properties and microstructure of selective-laser-melted AlSi10Mg alloys, Mater. Sci. Eng. A. 822 (2021) 141612. https://doi.org/10.1016/J.MSEA.2021.141612.
[59] W. Zhang, Y. Hu, X. Ma, G. Qian, J. Zhang, Z. Yang, F. Berto, Very-high-cycle fatigue behavior of AlSi10Mg manufactured by selected laser melting: Crystal plasticity modeling, Int. J. Fatigue. 145 (2021) 106109. https://doi.org/https://doi.org/10.1016/j.ijfatigue.2020.106109.
[60] Y. and D. Zhang Kunqing and Gu, Yejun and Chen, Wen and Morris Wang, Y. and El-Awady, Jaafar and McDowell, David L and Zhu, Ting, Modeling of microscale internal stresses in additively manufactured stainless steel, Model. Simul. Mater. Sci. Eng. (2022). http://iopscience.iop.org/article/10.1088/1361-651X/ac8698.
[61] N. Takata, M. Liu, H. Kodaira, A. Suzuki, M. Kobashi, Anomalous strengthening by supersaturated solid solutions of selectively laser melted Al–Si-based alloys, Addit. Manuf. 33 (2020) 101152. https://doi.org/10.1016/J.ADDMA.2020.101152.
[62] M. Liu, N. Takata, A. Suzuki, M. Kobashi, M. Kato, Enhancement in strength and ductility of laser powder bed fused Al–12Si alloy by introducing nanoscale precipitates, Addit. Manuf. Lett. 1 (2021) 100008. https://doi.org/10.1016/J.ADDLET.2021.100008.
[63] Y.M. Wang, T. Voisin, J.T. McKeown, J. Ye, N.P. Calta, Z. Li, Z. Zeng, Y. Zhang, W. Chen, T.T. Roehling, R.T. Ott, M.K. Santala, P.J. Depond, M.J. Matthews, A. V. Hamza, T. Zhu, Additively manufactured hierarchical stainless steels with high strength and ductility, Nat. Mater. (2018). https://doi.org/10.1038/NMAT5021.
[64] A. Hadadzadeh, C. Baxter, B.S. Amirkhiz, M. Mohammadi, Strengthening mechanisms in direct metal laser sintered AlSi10Mg: Comparison between virgin and recycled powders, Addit. Manuf. 23 (2018) 108–120. https://doi.org/10.1016/J.ADDMA.2018.07.014.
[65] Y. Wang, Y. Zhao, X. Xu, D. Pan, W. Jiang, X. Yang, Z. Wang, Superior mechanical properties induced by the interaction between dislocations and precipitates in the electro-pulsing treated Al-Mg-Si alloys, Mater. Sci. Eng. A. 735 (2018) 154–161. https://doi.org/https://doi.org/10.1016/j.msea.2018.08.029.

[66] A. Hadadzadeh, B.S. Amirkhiz, J. Li, A. Odeshi, M. Mohammadi, Deformation mechanism during dynamic loading of an additively manufactured AlSi10Mg_200C, Mater. Sci. Eng. A. 722 (2018) 263–268. https://doi.org/https://doi.org/10.1016/j.msea.2018.03.014.
[67] A. Mazahery, M.O. Shabani, Modification Mechanism and Microstructural Characteristics of Eutectic Si in Casting Al-Si Alloys: A Review on Experimental and Numerical Studies, JOM. 66 (2014) 726–738. https://doi.org/10.1007/s11837-014-0968-1.
[68] R. Haghayeghi, G. Timelli, An investigation on primary Si refinement by Sr and Sb additions in a hypereutectic Al-Si alloy, Mater. Lett. 283 (2021) 128779. https://doi.org/https://doi.org/10.1016/j.matlet.2020.128779.
[69] J. Abboud, J. Mazumder, Developing of nano sized fibrous eutectic silicon in hypereutectic Al–Si alloy by laser remelting, Sci. Rep. 10 (2020) 12090. https://doi.org/10.1038/s41598-020-69072-1.
[70] C.H. Liu, J.H. Chen, C. Li, C.L. Wu, D.Z. Li, Y.Y. Li, Multiple silicon nanotwins formed on the eutectic silicon particles in Al–Si alloys, Scr. Mater. 64 (2011) 339–342. https://doi.org/https://doi.org/10.1016/j.scriptamat.2010.10.030.
[71] S. Mahajan, Critique of mechanisms of formation of deformation, annealing and growth twins: Face-centered cubic metals and alloys, Scr. Mater. 68 (2013) 95–99. https://doi.org/https://doi.org/10.1016/j.scriptamat.2012.09.011.
[72] M. Liu, K. Wei, R. Zhou, X. Yue, X. Zeng, Microstructure and mechanical property of high power laser powder bed fusion AlSi10Mg alloy before and after T6 heat treatment, Virtual Phys. Prototyp. 17 (2022) 749–767. https://doi.org/10.1080/17452759.2022.2068294.
[73] D.K. Kim, J.H. Hwang, E.Y. Kim, Y.U. Heo, W. Woo, S.H. Choi, Evaluation of the stress-strain relationship of constituent phases in AlSi10Mg alloy produced by selective laser melting using crystal plasticity FEM, J. Alloys Compd. 714 (2017) 687–697. https://doi.org/10.1016/J.JALLCOM.2017.04.264.
[74] M.F. Ashby, The deformation of plastically non-homogeneous materials, Philos. Mag. (1970). https://doi.org/10.1080/14786437008238426.
[75] A. Salandari Rabori, V. Fallah, Room temperature strain rate sensitivity of as-built 3D printed AlSi10Mg by laser powder bed fusion, Mater. Lett. 320 (2022) 132395. https://doi.org/https://doi.org/10.1016/j.matlet.2022.132395.
[76] B. Gwalani, M. Olszta, S. Varma, L. Li, A. Soulami, E. Kautz, S. Pathak, A. Rohatgi, P. V Sushko, S. Mathaudhu, C.A. Powell, A. Devaraj, Extreme shear-deformation-induced modification of defect structures and hierarchical microstructure in an Al–Si alloy, Commun. Mater. 1 (2020) 85. https://doi.org/10.1038/s43246-020-00087-x.
[77] D. Farkas, Deformation behavior of a model high entropy alloy from atomistic simulations, Mater. Sci. Eng. A. 812 (2021) 141124. https://doi.org/https://doi.org/10.1016/j.msea.2021.141124.
[78] S. Zhao, B. Kad, E.N. Hahn, B.A. Remington, C.E. Wehrenberg, C.M. Huntington, H.-S. Park, E.M. Bringa, K.L. More, M.A. Meyers, Pressure and shear-induced amorphization of silicon, Extrem. Mech. Lett. 5 (2015) 74–80. https://doi.org/https://doi.org/10.1016/j.eml.2015.10.001.
[79] J. Tu, L. Liu, Y. Dou, C. Huang, L. Tan, L. Hu, Q. Sun, Z. Zhou, Deformation and annealing behaviors of as-cast non-equiatomic high entropy alloy, Mater. Sci. Eng. A. 737 (2018) 9–17. https://doi.org/https://doi.org/10.1016/j.msea.2018.08.109.
[80] S. V Bobylev, A.K. Mukherjee, I.A. Ovid'ko, Emission of partial dislocations from amorphous intergranular boundaries in deformed nanocrystalline ceramics, Scr. Mater. 60 (2009) 36–39. https://doi.org/https://doi.org/10.1016/j.scriptamat.2008.08.025.
[81] Q. Fang, L. Zhang, Emission of partial dislocations in silicon under nanoindentation, J. Mater. Res. 28 (2013) 1995–2003. https://doi.org/DOI: 10.1557/jmr.2013.189.
[82] Y. Cao, L.C. Zhang, Y. Zhang, Twinning interactions induced amorphisation in ultrafine silicon grains, Mater. Sci. Eng. A. 658 (2016) 321–325. https://doi.org/https://doi.org/10.1016/j.msea.2016.02.014.

[83] J. Wang, H. Huang, Shockley partial dislocations to twin: Another formation mechanism and generic driving force, Appl. Phys. Lett. 85 (2004) 5983–5985. https://doi.org/10.1063/1.1835549.
[84] S. Dong, J. Zhou, D. Hui, X. Pang, Q. Wang, S. Zhang, L. Wang, Interaction between edge dislocations and amorphous interphase in carbon nanotubes reinforced metal matrix nanocomposites incorporating interface effect, Int. J. Solids Struct. 51 (2014) 1149–1163. https://doi.org/https://doi.org/10.1016/j.ijsolstr.2013.12.011.
[85] H. Chen, V.I. Levitas, L. Xiong, Amorphization induced by 60° shuffle dislocation pileup against different grain boundaries in silicon bicrystal under shear, Acta Mater. 179 (2019) 287–295. https://doi.org/https://doi.org/10.1016/j.actamat.2019.08.023.
[86] J. George, S. Mannepalli, K.S.R.N. Mangalampalli, Understanding Nanoscale Plasticity by Quantitative In Situ Conductive Nanoindentation, Adv. Eng. Mater. 23 (2021) 2001494. https://doi.org/https://doi.org/10.1002/adem.202001494.
[87] H. Idrissi, P. Carrez, P. Cordier, On amorphization as a deformation mechanism under high stresses, Curr. Opin. Solid State Mater. Sci. 26 (2022) 100976. https://doi.org/https://doi.org/10.1016/j.cossms.2021.100976.
[88] S.K. Mohapatra, V. Ranjan, S. Tripathy, Study of severe plastic deformations of metallic materials:- A move towards Amorphization, Mater. Today Proc. 56 (2022) 735–741. https://doi.org/https://doi.org/10.1016/j.matpr.2022.02.244.
[89] L. Zhao, L. Song, J.G. Santos Macías, Y. Zhu, M. Huang, A. Simar, Z. Li, Review on the correlation between microstructure and mechanical performance for laser powder bed fusion AlSi10Mg, Addit. Manuf. 56 (2022) 102914. https://doi.org/https://doi.org/10.1016/j.addma.2022.102914.
[90] M. Albu, R. Krisper, J. Lammer, G. Kothleitner, J. Fiocchi, P. Bassani, Microstructure evolution during in-situ heating of AlSi10Mg alloy powders and additive manufactured parts, Addit. Manuf. 36 (2020) 101605. https://doi.org/https://doi.org/10.1016/j.addma.2020.101605.
[91] M. Garcia-Lechuga, N. Casquero, A. Wang, D. Grojo, J. Siegel, Deep Silicon Amorphization Induced by Femtosecond Laser Pulses up to the Mid-Infrared, Adv. Opt. Mater. 9 (2021) 2100400. https://doi.org/https://doi.org/10.1002/adom.202100400.
[92] W. Lefebvre, G. Rose, P. Delroisse, E. Baustert, F. Cuvilly, A. Simar, Nanoscale periodic gradients generated by laser powder bed fusion of an AlSi10Mg alloy, Mater. Des. 197 (2021) 109264. https://doi.org/https://doi.org/10.1016/j.matdes.2020.109264.
[93] J.Y. Huang, H. Yasuda, H. Mori, Deformation-induced amorphization in ball-milled silicon, Philos. Mag. Lett. 79 (1999) 305–314. https://doi.org/10.1080/095008399177147.
[94] Y. Cao, L.C. Zhang, Y. Zhang, Twinning interactions induced amorphisation in ultrafine silicon grains, Mater. Sci. Eng. A. 658 (2016) 321–325. https://doi.org/10.1016/J.MSEA.2016.02.014.
[95] Z. Zhang, F. Meng, J. Cui, B. Wang, Z. Wang, Y. Lu, H. ul Hassan, D. Guo, Deformation induced complete amorphization at nanoscale in a bulk silicon, AIP Adv. 9 (2019) 25101. https://doi.org/10.1063/1.5079819.
[96] D.R. Clarke, M.C. Kroll, P.D. Kirchner, R.F. Cook, B.J. Hockey, Amorphization and Conductivity of Silicon and Germanium Induced by Indentation, Phys. Rev. Lett. 60 (1988) 2156–2159. https://doi.org/10.1103/PhysRevLett.60.2156.
[97] S. Zhao, E.N. Hahn, B. Kad, B.A. Remington, C.E. Wehrenberg, E.M. Bringa, M.A. Meyers, Amorphization and nanocrystallization of silicon under shock compression, Acta Mater. 103 (2016) 519–533. https://doi.org/https://doi.org/10.1016/j.actamat.2015.09.022.
[98] S.O. Rogachev, R. V Sundeev, N.Y. Tabachkova, High pressure torsion-induced amorphous phase in a multilayer V-10Ti-5Cr/Zr-2.5Nb/V-10Ti-5Cr hybrid material, Mater. Lett. 234 (2019) 220–223. https://doi.org/https://doi.org/10.1016/j.matlet.2018.09.112.
[99] K. Madhav Reddy, A. Hirata, P. Liu, T. Fujita, T. Goto, M.W. Chen, Shear amorphization of boron suboxide, Scr. Mater. 76 (2014) 9–12. https://doi.org/https://doi.org/10.1016/j.scriptamat.2013.12.001.
[100] B.Y. Li, A.C. Li, S. Zhao, M.A. Meyers, Amorphization by mechanical deformation, Mater. Sci.

Eng. R Reports. 149 (2022) 100673. https://doi.org/https://doi.org/10.1016/j.mser.2022.100673.
[101] T.D. Shen, C.C. Koch, T.L. McCormick, R.J. Nemanich, J.Y. Huang, J.G. Huang, The structure and property characteristics of amorphous/nanocrystalline silicon produced by ball milling, J. Mater. Res. 10 (1995) 139–148. https://doi.org/10.1557/JMR.1995.0139.
[102] V. Domnich, Y. Gogotsi, S. Dub, Effect of phase transformations on the shape of the unloading curve in the nanoindentation of silicon, Appl. Phys. Lett. 76 (2000) 2214–2216. https://doi.org/10.1063/1.126300.
[103] Y. Wang, J. Zou, H. Huang, L. Zhou, B.L. Wang, Y.Q. Wu, Formation mechanism of nanocrystalline high-pressure phases in silicon during nanogrinding., Nanotechnology. 18 (2007) 465705. https://doi.org/10.1088/0957-4484/18/46/465705.
[104] V.G. Pushin, R.Z. Valiev, Y.T. Zhu, D. V Gunderov, A. V Korolev, N.I. Kourov, T.E. Kuntsevich, E.Z. Valiev, L.I. Yurchenko, Severe Plastic Deformation of Melt-Spun Shape Memory Ti₂NiCu and Ni₂MnGa Alloys, Mater. Trans. 47 (2006) 546–549. https://doi.org/10.2320/matertrans.47.546.
[105] R. V Sundeev, A.M. Glezer, A. V Shalimova, Crystalline to amorphous transition in solids upon high-pressure torsion, J. Alloys Compd. 611 (2014) 292–296. https://doi.org/https://doi.org/10.1016/j.jallcom.2014.05.109.
[106] M. Albu, S. Mitsche, M. Nachtnebel, R. Krisper, M. Dienstleder, H. Schröttner, G. Kothleitner, Microstructure Investigations of Powders and Additive Manufactured Parts, BHM Berg- Und Hüttenmännische Monatshefte. 165 (2020) 169–174. https://doi.org/10.1007/s00501-020-00958-3.
[107] J. Li, J. Sun, Y. Li, G. Qian, Z. Wang, Very-high-cycle fatigue induced growth and amorphization of Si particles in additively manufactured AlSi10Mg alloy: Dependence of applied stress ratio, Int. J. Fatigue. 164 (2022) 107167. https://doi.org/https://doi.org/10.1016/j.ijfatigue.2022.107167.
[108] J. Crain, G.J. Ackland, J.R. Maclean, R.O. Piltz, P.D. Hatton, G.S. Pawley, Reversible pressure-induced structural transitions between metastable phases of silicon, Phys. Rev. B. 50 (1994) 13043–13046. https://doi.org/10.1103/PhysRevB.50.13043.
[109] X.X. Zhang, A. Lutz, H. Andrä, M. Lahres, W.M. Gan, E. Maawad, C. Emmelmann, Evolution of microscopic strains, stresses, and dislocation density during in-situ tensile loading of additively manufactured AlSi10Mg alloy, Int. J. Plast. 139 (2021) 102946. https://doi.org/10.1016/J.IJPLAS.2021.102946.
[110] O. Shikimaka, A. Prisacaru, Deformation mechanisms under nanoscratching of Si: effect of scratching speed, load and indenter orientation, Mater. Res. Express. 6 (2019) 85011. https://doi.org/10.1088/2053-1591/ab1a0d.
[111] X. Wu, N. Tao, Y. Hong, J. Lu, K. Lu, Localized solid-state amorphization at grain boundaries in a nanocrystalline Al solid solution subjected to surface mechanical attrition, J. Phys. D. Appl. Phys. 38 (2005) 4140–4143. https://doi.org/10.1088/0022-3727/38/22/019.
[112] H. Chen, S. Patel, M. Vlasea, Y. Zou, Enhanced tensile ductility of an additively manufactured AlSi10Mg alloy by reducing the density of melt pool boundaries, Scr. Mater. 221 (2022) 114954. https://doi.org/https://doi.org/10.1016/j.scriptamat.2022.114954.
[113] D.D. Ben, Y.R. Ma, H.J. Yang, L.X. Meng, X.H. Shao, H.Q. Liu, S.G. Wang, Q.Q. Duan, Z.F. Zhang, Heterogeneous microstructure and voids dependence of tensile deformation in a selective laser melted AlSi10Mg alloy, Mater. Sci. Eng. A. 798 (2020) 140109. https://doi.org/10.1016/J.MSEA.2020.140109.
[114] J. Delahaye, J.T. Tchuindjang, J. Lecomte-Beckers, O. Rigo, A.M. Habraken, A. Mertens, Influence of Si precipitates on fracture mechanisms of AlSi10Mg parts processed by Selective Laser Melting, Acta Mater. (2019). https://doi.org/10.1016/j.actamat.2019.06.013.
[115] L. Song, L. Zhao, L. Ding, Y. Zhu, M. Huang, A. Simar, Z. Li, Microstructure and loading direction dependent hardening and damage behavior of laser powder bed fusion AlSi10Mg, Mater. Sci. Eng. A. 832 (2022) 142484. https://doi.org/https://doi.org/10.1016/j.msea.2021.142484.

[116] J.M. Park, J. Choe, H.K. Park, S. Son, J. Jung, T.-S. Kim, J.-H. Yu, J.G. Kim, H.S. Kim, Synergetic strengthening of additively manufactured (CoCrFeMnNi)99C1 high-entropy alloy by heterogeneous anisotropic microstructure, Addit. Manuf. 35 (2020) 101333. https://doi.org/https://doi.org/10.1016/j.addma.2020.101333.
[117] C.L. Chen, A. Richter, R.C. Thomson, Mechanical properties of intermetallic phases in multi-component Al-Si alloys using nanoindentation, Intermetallics. (2009). https://doi.org/10.1016/j.intermet.2009.02.003.
[118] G.M. Karthik, E.S. Kim, A. Zargaran, P. Sathiyamoorthi, S.G. Jeong, H.S. Kim, Role of cellular structure on deformation twinning and hetero-deformation induced strengthening of laser powder-bed fusion processed CuSn alloy, Addit. Manuf. 54 (2022) 102744. https://doi.org/https://doi.org/10.1016/j.addma.2022.102744.
[119] Y. Ma, M. Yang, F. Yuan, X. Wu, A Review on Heterogeneous Nanostructures: A Strategy for Superior Mechanical Properties in Metals, Metals (Basel). 9 (2019). https://doi.org/10.3390/met9050598.
[120] R. Jain, M. Yadava, N. Nayan, N.P. Gurao, Combinatorial synchrotron diffraction-constitutive modelling-crystal plasticity simulation framework for direct metal laser sintered AlSi10Mg alloy, Materialia. 22 (2022) 101395. https://doi.org/https://doi.org/10.1016/j.mtla.2022.101395.
[121] H. Mughrabi, Dislocation wall and cell structures and long-range internal stresses in deformed metal crystals, Acta Metall. (1983). https://doi.org/10.1016/0001-6160(83)90007-X.
[122] J.Y. Zhang, B. Xu, N. ul H. Tariq, M.Y. Sun, D.Z. Li, Y.Y. Li, Effect of strain rate on plastic deformation bonding behavior of Ni-based superalloys, J. Mater. Sci. Technol. 40 (2020) 54–63. https://doi.org/https://doi.org/10.1016/j.jmst.2019.08.044.
[123] D.-K. Kim, W. Woo, J.-H. Hwang, K. An, S.-H. Choi, Stress partitioning behavior of an AlSi10Mg alloy produced by selective laser melting during tensile deformation using in situ neutron diffraction, J. Alloys Compd. 686 (2016) 281–286. https://doi.org/https://doi.org/10.1016/j.jallcom.2016.06.011.
[124] J. Wu, X.Q. Wang, W. Wang, M.M. Attallah, M.H. Loretto, Microstructure and strength of selectively laser melted AlSi10Mg, Acta Mater. (2016). https://doi.org/10.1016/j.actamat.2016.07.012.